Int. J. Multiphase Flow Vol. 12, No. 1, pp. 1–34, 1986
Printed in Great Britain.

0301–9322/86 $3.00 + .00

SINGLE-EXPOSURE NEUTRON TOMOGRAPHY OF TWO-PHASE FLOW†

E. M. A. HUSSEIN‡ and D. A. MENELEY‡
Nuclear Group–Design and Development Division, Ontario Hydro, Toronto, Ontario M5G 1X6, Canada

and

S. BANERJEE
Department of Chemical and Nuclear Engineering, University of California, Santa Barbara, CA 93106, U.S.A.

(*Received* 5 *March* 1984; *in revised form* 16 *May* 1985)

Abstract—A method is presented for measuring the phase density distribution at a cross-section of a gas–liquid flow system. The method utilizes the information carried by measured fluences of scattered fast neutrons. Reconstruction of the local density distribution is viewed as an inverse problem and a numerical method is developed for solving this problem. The physical and practical aspects of the problem are considered and some numerical and experimental results are presented.

1. INTRODUCTION

The behaviour of a two-phase system depends to a large extent on the manner on which the two phases are distributed in the system. Phase distribution (or equivalently flow regime), affects the interfacial and wall transfer of mass, momentum and heat. It also affects the structure of the average conservation equations used in separated flow models to describe the dynamics of the two phases. The conservation equations are coupled through interfacial transfer relationships for mass, momentum and heat as discussed, for example, by Banerjee & Chan (1980). These models are needed for the analysis of two-phase systems when departures from homogenous equilibrium flow are important. For development of such models, measurement of local mixture density (or void fraction) is desirable.

Existing techniques for phase distribution measurements can be divided into two categories: intrusive (probe-based) or nonintrusive (usually radiation-based). Intrusive methods such as impedance probes, hot film anemometry, microthermocouples and optical probes, though they may have fast response and relative simplicity of operation, cause flow disturbance. Light transmittance and scattering techniques can also be used, but in addition to their incapability of penetrating metallic walls, they are expensive and difficult to apply.

Radiation techniques for phase distribution measurements depend either on attenuation or scattering of the penetrating radiation. Techniques based on attenuation provide an estimate of the chordal void-fraction across the radiation path. A set of chordal void-fractions obtained at different intersecting radiation paths is then unfolded to obtain the phase distribution as shown by Zakaib *et al.* (1978) and Hau & Banerjee (1981). This process requires multiple exposure of the test section to the radiation source. Scattering techniques depend on the fact that, in a gas–liquid flow, only the liquid phase scatters radiation at a rate proportional to the phase content. Gamma-ray scattering techniques have been explored for phase distribution measurements, see for example Kondic *et al.* (1983). Since gamma-rays interact with the electrons of the matter, they may be more sensitive to the flow-containing walls (usually metal) than to the flow itself. Consequently, they have poor sensitivity when applied to high pressure systems. On the other hand, neutrons, particularly those of high energy, are more affected by the flow material than by the pipe

---

†Part of this work was done at McMaster University.

‡Present address: Department of Chemical Engineering, University of New Brunswick, P.O. Box 4400, Fredericton, N.B., Canada E3B 5A3.

metal and have higher interaction probability with hydrogeneous flow than gamma-rays. Therefore, fast neutrons are more suited for application in high-pressure systems and are expected to provide better sensitivity in transient measurements than gamma-rays.

Powerful 14-MeV neutron generators have become relatively inexpensive and readily available. They have been used for time-of-flight flow measurement (see Perez-Griffo *et al.* 1982) among others. This ready availability of equipment, coupled with the potential sensitivity of a neutron scattering technique, have motivated us to develop a method for cross-sectional phase distribution measurements. Since many interesting gas–liquid flows have a fluctuating or transient character, we decided to develop a technique based on a short single exposure of the test section. The single-exposure neutron tomography (SENT) technique is described in detail in Hussein's thesis (1983) and preliminary information and some experimental details have been presented by Hussein *et al.* (1983,1984). This paper discusses the theoretical aspects of the technique and presents some experimental and numerical results. The technique is briefly described below as a prelude to the theoretical aspects of the problem.

Figure 1 shows a schematic of the proposed SENT technique. A test section of the two-phase flow is exposed to a beam of 14-MeV neutrons, while a set of detectors surrounding the test section is used to measure the energy spectrum of the scattered neutrons. From the measurements, the void fraction (or equivalently the liquid fraction) inside each of the cells of a fictitious mesh constructed in the exposed section is to be determined. In the present work steam–water flow is considered; however, the SENT technique can be applied to most gas–liquid flows. Because of the unique relationship between the energy and angle of single elastic scatterings by the hydrogen in the flow stream, the energy of the detected neutrons provides information primarily on the location of water in the test section. On the other hand, the magnitude of the detector response provides information on the amount of water. Therefore, it is possible in principle to reconstruct the void distribution from the measured detector responses. The problem may be viewed as determining the unknown void (or liquid) fractions in the N cells of the fictitious mesh shown

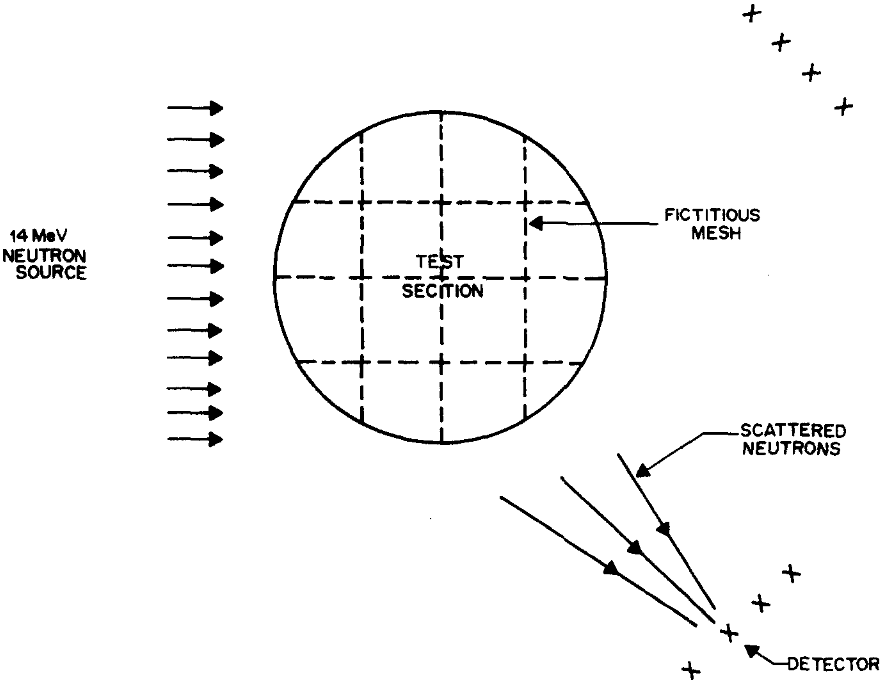

Figure 1. Schematic configuration of the SENT technique.

in figure 1. Then at least N independent measurements are needed in order to obtain the N unknowns. This is an inverse problem since one is trying to obtain a set of parameters (void fractions) from a set of results (detector responses). Functional analysis allows this inverse problem to be approached systematically, as shown by Hussein (1983). Such an approach elucidates the essential difficulties. Once these difficulties are identified and the strategy for solving them is established, then the physical and numerical details can be worked out. The mathematical fundamentals of the SENT inverse problem are outlined in section 2, while section 3 discusses the physical aspects. The mathematical and physical aspects are implemented in a numerical algorithm presented in section 4. The experimental techniques used for obtaining the required measurements are described in section 5. The application of the SENT technique for reconstructing the phase distribution for different flow regimes is illustrated in section 6.

2. THE INVERSE PROBLEM

In order to define the inverse problem, one has to define first the direct (or forward problem). As defined by Chadan & Sabatier (1977), the direct problem is the mapping of a set of theoretical "parameters" into a set of experimentally measurable "results." Solving the direct problem is then to obtain "computed results" from given "parameters." Conversely, obtaining the "parameters" from given measured "results" is called solving the inverse problem.

Clearly, the SENT problem is an inverse problem where the sought theoretical "parameters" are the local void fractions at designated cells in the test section, and the set of "results" consists of the measured scattered neutron fluences. Detailed functional analysis of this inverse problem guided by the analysis of Sabetier (1978) is given in Hussein (1983). Here only the essential aspects that aid in the practical solution of the problem are presented.

The first step in solving an inverse problem is to construct the direct problem, otherwise no solution to the inverse problem can be found. In other words, one has to find a physical model that relates the theoretical "parameters" to the measurements. Once this is done, the direct mapping can be constructed.

The direct mapping of the SENT problem can be defined as

$$\mathbf{m}: \rho \longrightarrow \mathbf{S}, \qquad [1]$$

where ρ is a vector representing the sought water fractions:

$$\rho = [\rho_1, \rho_2, \ldots, \rho_1, \ldots \rho_N]^T, \qquad [2]$$

where ρ_i is the water fraction in the ith cell of the mesh of figure 1, N is the number of cells in the mesh and S is a vector constructed from the known measurements:

$$\mathbf{S} = [S_1, S_2, \ldots, S_i, \ldots, S_M]^T, \qquad [3]$$

where S_i is the ith measurement and M is the number of available measurements (M is assumed to be greater than or equal to N).

Obviously one cannot construct the mapping $\mathbf{m}$, unless the nature of the "results" are precisely defined. The detectors shown schematically in figure 1 would count the number of neutrons scattered by the flow material in the test section. If one considers a measurement as the total number of neutrons arriving to the detector within a specified time interval, the vector ρ would then be related to the measurements through a complicated physical model (the neutron transport equation) and no simple formulation of the mapping $\mathbf{m}$ could be possible. A simple expression for $\mathbf{m}$ is desirable in order to facilitate the construction of its inverse. As we will show, by imposing some physical constraints and by selective measurement of the scattered neutrons, it is possible to obtain a matrix formulation of the direct mapping. This is provided by the single scattering model (SSM) of the problem. The SSM is discussed in detail in section 3.

With the mapping being presented by a matrix, relationship [1] can be rewritten as

$$\mathbf{S} = \mathbf{A}\,\rho, \tag{4}$$

where $\mathbf{A}$ is an $(M \times N)$ matrix that represents the direct mapping of the SENT problem.

In practical applications, the vector S is known approximately since it is obtained from measurements. Let $\tilde{\mathbf{S}}$ denote its approximate value. In such cases, one can speak only of finding an approximate solution of the equation

$$\mathbf{A}\rho = \tilde{\mathbf{S}}. \tag{5}$$

Usually, one cannot take for the approximate solution the result $\rho = \mathbf{A}^{-1}\tilde{\mathbf{S}}$, for two reasons: First, such a solution may not exist in the set of solutions defined by the closed interval [0,1] that contains all physically possible water fractions. Second, even if such a solution does exist, it may not possess the property of stability, that is, a small change in $\tilde{\mathbf{S}}$ may result in a large change in ρ. However, with the aid of supplementary information on the nature of the solution, one can select an appropriate "quasisolution."

One can obtain a quasisolution by minimizing, for example, the residuals of the problem as expressed by the cost function D_2^2 defined by

$$D_2^2 = \sum_{i=1}^{M} w_i^2 \left(S_i - \sum_{j=1}^{N} a_{ij}\rho_j \right)^2, \tag{6}$$

where a_{ij}'s are elements of the matrix $\mathbf{A}$ and w_i's are the reciprocals of the measurement variances. The quasisolution, ρ, that minimizes the above function is called the "least-squares" solution and is given by

$$\hat{\rho} = (\mathbf{A}^T\mathbf{W}\mathbf{A})^{-1}\mathbf{A}^T\mathbf{W}\tilde{\mathbf{S}}, \tag{7}$$

where $\mathbf{A}^T$ is the transpose of $\mathbf{A}$ and $\mathbf{W}$ is a diagonal matrix whose elements are the w_i's.

The physical constraint that the vectors ρ must be contained in the closed interval [0,1] is not necessarily met by the "least-squares" inverse mappings.

In order to construct mappings that result in physically acceptable solutions, one can rely on the so-called "regularization" methods to construct "constraint" mappings. There are many regularization methods, and a good survey of these methods can be found in the book by Tikhonov & Arsenin (1977).

In the SENT problem the "constraint" matrix is constructed such that the set of solutions is bounded by a weak upper bound of the solution and is given by

$$q_i = \min_j \frac{S_j + \sigma_j}{a_{ji}}, \quad a_{ji} \neq 0, \tag{8}$$

where q_i is the ith element of the weak upper bound vector $\mathbf{q}$,σ_j is the standard deviation of the measurement $\tilde{S}_j$ and a_{ji}'s are elements of the matrix $\mathbf{A}$ that defines the direct mapping $\mathbf{m}$. The quasisolution is then constructed as shown by Hussein (1983) as

$$\hat{\rho} = [\mathbf{A}^T\mathbf{W}\mathbf{A} + (\tau^2/N)\mathbf{Q}^{-2}]^{-1}\mathbf{A}^T\mathbf{W}\tilde{\mathbf{S}}, \tag{9}$$

where $\mathbf{A}$ and $\mathbf{W}$ as defined following [6], while $\mathbf{Q}$ is a diagonal matrix whose elements are the elements of the weak upper bound vector $\mathbf{q}$ whose elements are defined by [8]. The parameter τ^2 is called the regularization parameter. The method used for deriving [9] is given in detail by Hussein (1983) following closely the approach of Burrus (1965). Miller (1970) had shown that the solution $\hat{\rho}$ of [9], is bounded and stable. However, there is no guarantee that the solution lies within the interval [0,1]. Nevertheless, by choosing the appropriate value of τ^2 one can contain the solution within this interval. A value of τ^2 equal to N appears to achieve this goal as will be shown in section 6.

The error associated with the quasisolution, $\hat{\rho}$, can be estimated from

$$\hat{\rho} - \rho = (\mathbf{m}_0^{-1}\mathbf{m} - \mathbf{1})\rho + \mathbf{m}_0^{-1}\epsilon,$$

with

$$\mathbf{m} \equiv \mathbf{A},$$

$$\hat{\rho} \equiv \mathbf{m}_0^{-1}\tilde{\mathbf{S}},$$

where ρ is the "exact" solution of the problem, $\mathbf{m}$ is the direct mapping, $\mathbf{m}_0^{-1}$ is the constructed inverse mapping and ϵ is the error associated with the measurements. Since ρ is not known, the right-hand side of the above equation can be expressed in terms of $\hat{\rho}$ resulting in the relationships

$$\hat{\rho} - \rho = (\mathbf{1} - \mathbf{m}^{-1}\mathbf{m}_0)\hat{\rho} + \mathbf{m}^{-1}\epsilon. \qquad [10]$$

Since $\mathbf{m}_0^{-1}$, rather than $\mathbf{m}^{-1}$, is constructed in the solution, the former can be used for $\mathbf{m}^{-1}$ in the above relationship, resulting in the error $\mathbf{m}_0^{-1}\epsilon$ in the solution. If ϵ is taken as the vector of the standard deviation of the measurements, then $\mathbf{m}_0^{-1}\epsilon$ would be the random error associated with the solution $\hat{\rho}$. A "bias" or resolving error may also result if the round-off error affects the inversion process. This error is expressed by $(\mathbf{1} - \mathbf{m}_0^{-1}\mathbf{m})\hat{\rho}$. A third type of error might exist if the direct mapping is not exact; that is, if the physical model of the problem does not reproduce exactly the "error-free" measurements, due to physical approximations. This is called physical error.

For the problem considered here, the resolving error is a round-off error and can be estimated for the method used for matrix inversion, given the precision of the computing machine. The physical error becomes significant only if the single scattering model used as a direct mapping ceases to be valid. The domain within which the model can be used is defined in the next section, together with a worst error estimate of the physical error. Therefore, the only error to be routinely calculated in the SENT problem is the random error $\mathbf{m}_0^{-1}\epsilon$.

3. PHYSICAL MODELING

As the previous section emphasizes, it is essential to construct the direct mapping in order to solve the inverse problem. This section shows how the direct mapping is developed from physical principles.

3.1 *Fundamentals*

In order to be able to develop an adequate physical model for the SENT technique, one has to examine the fundamental theory upon which the technique is based. The technique, as presented in section 1, utilizes the scattering of 14-MeV neutrons for providing information on the amount and distribution of the test section material. Therefore, the basis of the SENT technique is the neutron scattering process. The scattering magnitude for a gas–liquid flow system depends on the density and composition of the liquid phase. For a steam–water flow, the scattering elements are hydrogen and oxygen, and the density inside a scattering cell can be taken as the steam–water mixture density in the cell. For 14-MeV neutrons, the scattering process is mainly elastic; since scattering by hydrogen is always elastic and the inelastic cross-section of oxygen is negligible compared to its elastic cross-section (see Hughes & Schwartz 1958). Therefore, one can claim that the SENT technique, when applied to a steam–water flow, relies essentially on elastic scattering.

The kinematics of an elastic-scattering event for a neutron can be described by invoking laws of conservation of energy and linear momentum (see for example Henry 1975), leading to the relationship:

$$E_\theta = \frac{1}{2} E_0[(1 + \gamma) + (1 - \gamma)\cos\psi], \qquad [11]$$

where

$$\gamma = [(A - 1)/(A + 1)]^2,$$

and

$$\cos\theta = (A\cos\psi + 1)/(A^2 + 2A\cos\psi + 1)^{1/2},$$

with A being the mass number of the scattering nucleus, E_0 the energy of the incident neutron, and E_θ is the energy of the neutron after being scattered by an angle θ in the laboratory system (or ψ in the center-of-mass system). Equation [11] shows that there is a unique relationship between the energy and angle of scattering, for a given scattering material. Figure 2 shows this relationship plotted for some elements of interest ^{1}H, ^{2}H, ^{12}C and ^{16}O. For a steam–water system, scattering is caused by both ^{1}H and ^{16}O nuclei, which have different energy-angle relationships. However, as one can see from figure 2, if forward scattering at energy less than (15/17) E_0 is monitored, only scattering by hydrogen would be observed and no oxygen contribution would result. The (15/17) ratio is obtained from relationship [11] for oxygen ($A = 16$) at $\theta = 90°$ (larger values of θ lead to backward scattering). By monitoring only hydrogen scattering, one should be able to determine the location of the scattering material (steam–water) from the angle corresponding to the energy of the scattered neutrons. This unique angle-energy relationship is utilized in the SENT technique to link the energy of the measured (scattered) neutrons to the location of the material in the test section; keeping in mind that neutrons of energy larger than 12.35 MeV ($= 14$ MeV × 15/17) are excluded since they correspond to oxygen scattering.

Although [11] provides a useful relationship between the energy and angle of scattering, it does not predict the probable scattering angle. Such prediction requires the use of quantum mechanics combined with measurements. However, cross-section libraries report for each element a set of Legendre coefficients that can be utilized to estimate the probability of scattering to an angle θ, $P(\theta)$, as follows:

$$P(\theta) = \Sigma(E_0 \rightarrow E)/\Sigma_s(E) \sum_{L=0}^{\infty} \frac{1}{2}(2L + 1) f_L(E_0 \rightarrow E) P_L(\cos^{-1}\theta), \qquad [12]$$

where $\Sigma(E_0 \rightarrow E)$ is the transfer cross section from E_0 to E, $\Sigma_s(E)$ is the scattering cross section at E, f_L is the Lth Legendre polynomial, estimated at $\cos^{-1}\theta$. The above relationship assumes isotropic scattering in the azimuthal direction, which is a reasonable assumption for many materials. The summation in the above equation should be performed to the highest available order particularly for hydrogenous materials, to provide an adequate estimate for

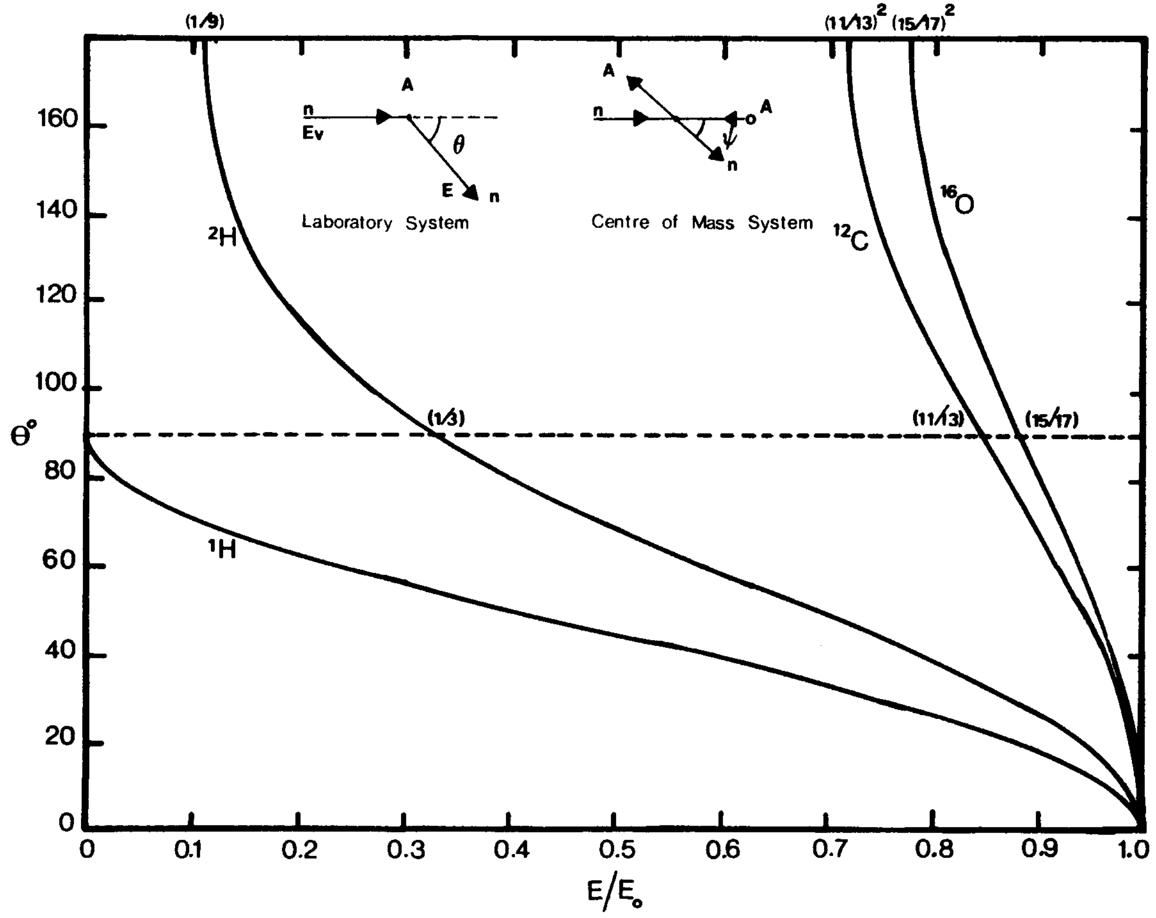

Figure 2. Relationship between energy and angle of scattering.

the scattering probability. The number of scattered neutrons is proportional to both the probability of scattering and the amount of available material. Therefore, knowing the scattering probability enables the estimation of the amount of scattering material by measuring the number of neutrons scattered.

Equations [11] and [12] are fundamental to the SENT technique. While the first equation relates the energy of the measured scattered neutrons to the location of the scattering material, the second equation can be used together with the measured number of scattered neutrons to provide an estimate of the amount of material present. A set of measurements covering the test section material can be then used to calculate the density distribution in the test section. However, one should keep in mind that the above two equations consider only single scattering. Therefore, if one measures neutrons that have suffered more than one collision before reaching the detector, one would not be able to utilize relationships [11] and [12] to relate the measurements to the location and amount of the scattering material. Therefore, minimizing or correcting for the contribution of multiple scattering to the measurements is a main concern in the SENT technique. This aspect is discussed in subsection 3.3. Before proceeding to discuss how these two fundamental equations are used to construct a physical model of the SENT problem, one should note that relationship [11], as plotted in figure 2, shows that the idea of SENT technique can be used not only in steam–water systems but in many other systems. For example, for a heavy water boiling two-phase flow, one would utilize the appropriate energy-angle relationship for ^{2}H and excludes scattering by oxygen. For a multicomponent flow such as oil–steam–water flow, by monitoring backward scattering below the energy of $(15/17)^2E_0$ (see figure 2), one can estimate the amount of carbon available. This, in addition to the forward scattering information and the flow chemical composition, could be used to determine the phase content (see Hussein 1984).

3.2 *The single scattering model*

The physical model required for solving the SENT inverse problem relates the local void fractions to the measurements (the direct mapping). The fundamental equations [11] and [12] discussed above are used in this subsection to formulate this model. Let us first define carefully both the local void fraction and the measurements.

The fundamental analysis, presented above, indicates that one is monitoring scattering by hydrogen. In a steam–water system, knowing the hydrogen content in a given volume leads directly to the mixture density in the volume, since the chemical composition is known. Therefore, in effect one is monitoring the steam–water mixture density. By dividing the test section into fictitious cells (see figure 3), the mixture's specific volume in a cell j is given by

$$(1/v_j) = (1 - \rho_j)(1/v_G) + \rho_j(1/v_L),$$

where ρ_j is the local liquid fraction in the cell and v_L and v_G are the liquid and vapour specific volumes, respectively. For many applications, v_L is at least an order of magnitude smaller than v_G and the first term in the above equation can be neglected. Then

$$\rho_j \simeq v_L/v_j; \qquad [13]$$

i.e., the local liquid fraction is equal to the ratio between the density of the steam–water mixture in the cell to its density if it was completely filled with the liquid phase (water). Therefore, the local water fraction, which is the complement of the local void-fraction, is proportional to the material density in the cell and can be used in conjunction with the fundamental relationships [11] and [12] to describe the physics of the neutron scattering

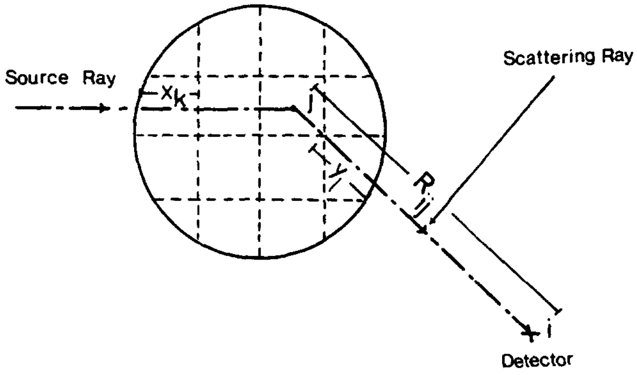

Figure 3. A fictitious mesh constructed in the test section and a typical neutron path.

mechanism. The N water fractions in the fictitious mesh of figure 3, are considered as the elements of a vector ρ of dimension N that represents the unknowns in the SENT problem.

The fundamental equations [11] and [12] indicate also that one has to measure the number of neutrons scattered by the hydrogen nuclei at a given energy. This can be obtained by measuring at a specific position the energy spectrum of the scattered neutrons, and excluding those energies that correspond to oxygen scattering. By dividing the measured spectrum into statistically appropriate energy intervals one can obtain a set of individual measurements, each corresponding to a particular scattering energy range (and consequently an angle interval) and each can be considered as an independent measurement in the SENT problem. By measuring the energy spectrum at another position one can obtain another set of independent measurements, since in the new position, new directions of scattering are observed. Therefore, the required number of measurements can be obtained by measuring the energy spectra of the scattered neutrons using a number of detectors located at different positions such that they monitor forward scattering, as required by the fundamental equations [11] and [12]. In addition to excluding energies that correspond to oxygen scattering, one has also to discard energies that result in scattering directions that do not correspond to scattering from inside the test section. More details on the design and arrangement of the detection system are given by Hussein *et al.* (1984). The collected set of measurements are arranged into an M-dimensional vector S whose elements are the individual measurements obtained from the energy spectra. For each element of the vector S, the corresponding energy range and the detector position have to be defined, to enable relating the energy to the direction of scattering from the test section. The dimensions M of the vector S must be larger than or equal to the dimensions of the unknown vector ρ, to avoid underdetermining the SENT problem.

The above definitions of the vectors ρ and S require the physical model relating ρ to S to be an $M \times N$ matrix. Let this matrix be **A**. Then

$$\mathrm{S} = \mathbf{A}\rho.$$

An element a_{ij} of **A** then defines the contribution of cell j to the measurement S_i. This definition of the matrix **A** enables the establishment of the physical model required for calculating the contribution of a cell j to a measurement S_i. To be consistent with the physical constraints of the fundamental equations [11] and [12], it is assumed that the measurements record only neutrons that have suffered a single collision inside the test section. This assumption is examined later. By following the path of a source neutron that suffers a collision in cell j and scatters towards the detector that records the measurement S_i (see figure 3) one can estimate the contribution of this neutron to S_i, and consequently a_{ij}, as follows:

$$
\begin{aligned}
a_{ij} = \ & [\text{number of incident source neutrons}] \\
& \times [\text{probability of reaching cell } j] \\
& \times [\text{probability of scattering by an angle } \theta \text{ that corresponds to the} \\
& \quad \text{energy at which } S_i \text{ is recorded}] \\
& \times [\text{probability of reaching the detector}].
\end{aligned}
\qquad [14]
$$

The probability of a source neutron reaching cell j without being scattered or absorbed in preceding cells depends on the density of these cells, and can be expressed as

$$
\text{probability of reaching cell } j = \exp\left[-\Sigma_0 \sum_k x_k \rho_k\right],
$$

where Σ_0 is the total cross-section of a source neutron in water, x_k is the distance the neutron travels in a preceding cell k and ρ_k is the water fraction in the cell. Note that $\Sigma_0 \rho_k$ represents the total cross-section of a source neutron crossing a cell of water fraction ρ_k. The probability that a neutron reaching cell j scatters by an angle θ, in order to contribute to the measurements S_i, is given by $P(\theta)$ (see [12]). The probability that a neutron being scattered at cell j will reach detector where S_i is recorded is given by:

$$
\exp\left(-\Sigma_i \sum_l y_l \rho_l\right) \cdot (1/2\,\pi R_{ij}^2),
$$

where Σ_i is the total cross section in water estimated at the detection energy, corresponding to S_i, y_l is the distance a neutron travels in a cell l on its way towards the detector, ρ_l is the water fraction in the cell and R_{ij} is the distance between cell j and the detector where S_i is recorded. The ($1/2\pi$) term accounts for the azimuthal direction, where isotropic scattering is assumed, while R_{ij}^2 accounts for neutron divergence.

Combining the above three probabilities together, one obtains:

$$
\begin{aligned}
a_{ij} &= W_j \exp\left[-\Sigma_0 \sum_k x_k \rho_k\right] P(\theta) \\
&\qquad \exp\left[-\Sigma_i \sum_l y_l \rho_l\right] (1/2\,\pi R_{ij}^2), \\
&= 0, \text{ if cell } j \text{ does not contribute to } S_i,
\end{aligned}
\qquad [15]
$$

where W_j is the number of source neutrons reaching cell j and the provision of setting a_{ij} equal to zero takes care of the case when cell j is not seen from the position of the detector where S_i is recorded. This indicates that if a cell j is not seen by any detector, a_{ij} would be equal to zero for all values of i and the matrix **A** would be singular. To avoid this, one has to make sure that each cell is seen by at least one detector.

One has to note that the physical model presented by the matrix **A**, whose elements are defined by [15], assumes that the neutron source is a well collimated neutron beam of a uniform profile. Corrections for the source angular and intensity distribution can be introduced easily through the W_j terms. Also, the fact that S_i is estimated over an energy range, rather than a specific energy, and consequently a range of scattering angles, rather than a specific angle θ, is not taken into consideration in the above model. However, this can be overcome by dividing the angular range into a number of intervals and estimating the corresponding element of the matrix **A** using a number of neutron paths, each corresponding to one of the angular intervals. An angular interval of 0.5° appears to be sufficient for this purpose, as shown by Hussein *et al.* (1983). The model also assumes that the material inside any cell j is a homogeneous material of density ($\approx \rho_j/v_L$), where v_L is the liquid specific volume. Therefore, the model is more accurate for small cells than for large ones. The results of this single scattering model (SSM) are compared to the more elaborate Monte Carlo simulations in the following subsection. The Monte Carlo simulations were carried out using an approach similar to that previously reported by the authors, Banerjee *et al.* (1979). Note that the Monte Carlo simulations provides a more accurate direct mapping, but it does not solve the inverse problem.

3.3 *Verification of the SSM*

The two main sources of error in the SSM, as indicated above, are the contribution of multiple scattering and the effect of material homogenization in the cells. These two sources are investigated by comparing the results of the SSM to those of Monte Carlo simulation where multiple scattering is accounted for and no cell homogenization is done.

3.3.1 *Multiple scattering.* The average distance a neutron travels before suffering a collision is given by its mean-free path in the material. Therefore, by limiting the size of the test section to the order of magnitude of the mean-free path, the probability of multiple scattering would be significantly reduced. Moreover, since the average energy loss per neutron collision with hydrogen is half the original energy, the multiscattered neutrons would tend to score into the lower energy range of the detector. Therefore, by discounting low-energy neutrons from the measurements used in the SENT technique, the contribution of neutron multiple scattering is further reduced. As shown by Hussein *et al.* (1983), an energy of 3.5 MeV is recommended as the threshold energy below which measurements should be discarded. This energy is one fourth of the source energy (14 MeV) and corresponds to the average energy of a source neutron that suffers two collisions with hydrogen.

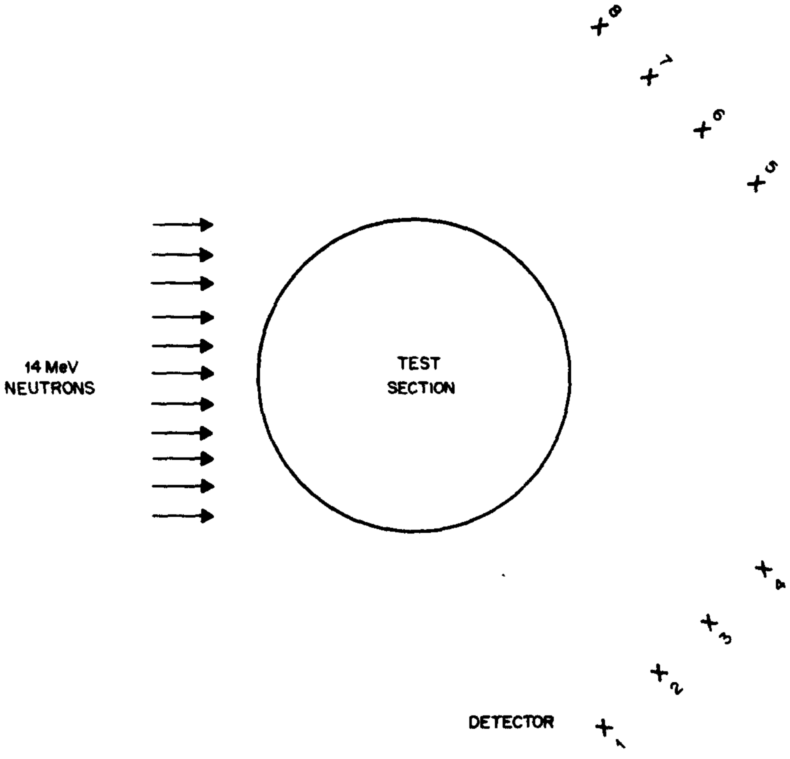

Figure 4. Detectors arrangement used in the Monte Carlo simulations.

Let us consider the case of a test section of a diameter equal to one mean-free path of the 14-MeV source neutrons, i.e. around 100 mm. Multiple scattering is expected to be largest when the test section is completely filled with water. Consider a set of four detectors located at one side of the test section downstream of a 14-MeV neutron beam as shown in figure 4. For each detector, the energy spectrum of the scattered neutrons is observed within the energy intervals [10.5,8.2], [8.2,5.8], and [5.8,3.5] MeV, which correspond to [30,40], [40,50], [50,60] degrees of scattering, respectively. These relatively wide energy intervals were used in the Monte Carlo simulation in order to obtain good statistics at a relatively low computer cost. Table 1 shows the fluence of the scattered neutrons for these detectors within the three energy (angular) intervals as calculated by the Monte Carlo method and the SSM. In the latter, 21 neutron paths (one per 0.5° of scattering) were used for each detector. Both a 4 × 4 grid and an 8 × 8 grid were used in the SSM in order to show the effect of the cell size on the model, since the detector fluence is calculated in the SSM by summing the contributions of the individual cells. As table 1 shows, the results of SSM lie within the error range of the corresponding Monte Carlo results, and reduction of the cell size seems to slightly improve the SSM results. For detection energies below 3.5 meV (excluded in the SENT technique), the SSM results do not agree well with the corresponding Monte Carlo results. Low-energy neutrons are more susceptible to rescattering than those of high energy; consequently a smaller portion of single-scattered low-energy neutrons succeed in reaching the detectors. On the other hand, some multiscattered neutrons may succeed in reaching the detectors at low energy because of the successive loss of energy in the scattering process. Therefore, the low-energy bands of the detectors are more influenced by multiple scattering, and the SSM is not adequate for estimating the neutron fluences at these energies. High-energy bands are also susceptible to multiple scattering effects, particularly by

Table 1. Monte Carlo and single scattering model fluences for a 100-mm "full of water" test section

Detector Number	MeV Scattering Energy Interval	10^6 x Fluence (Neutrons/cm^2/source neutron) Monte Carlo	4 x 4 Mesh	8 x 8 Mesh
1	10.5 - 8.2	22.96 (5.66)*	22.89 (0.3)+	23.51 (2.4)+
2	10.5 - 8.2	20.584 (6.4)	20.09 (2.45)	20.38 (0.99)
3	10.5 - 8.2	13.672 (7.88)	12.96 (5.21)	13.09 (4.26)
1	8.2 - 5.8	37.413 (4.7)	36.46 (2.55)	37.04 (1.0)
2	8.2 - 5.8	42.654 (5.1)	40.16 (5.85)	40.81 (4.32)
3	8.2 - 5.8	33.797 (4.5)	31.19 (4.75)	32.57 (3.63)
4	8.2 - 5.8	20.791 (3.6)	20.52 (1.30)	20.65 (0.68)
2	5.8 - 3.5	36.424 (5.6)	35.77 (.80)	36.19 (0.64)
3	5.8 - 3.5	38.341 (5.7)	36.20 (1.58)	36.51 (4.78)
4	5.8 - 3.5	28.696 (5.7)	28.04 (2.29)	28.29 (2.32)

* Fractional standard deviation (%)

\+ Fractional error relative to Monte Carlo (%)

Table 2. Relative weight of multiple scattering in a 100-mm "full of water" test section

E_p	11.1	9.1	7.4	6.1	4.4	3.9
R	5.4	5.5	3.1	4.9	3.8	7.0

E_p = Neutron Energy Prior to Scattering, MeV

R = (Weight of Rescattered Neutron/Total Weight of Scattered Neutrons) x 100

neutrons that suffer the first collision with oxygen, causing small energy degradation, and reach the detector by further rescattering. (Note, neutrons that suffer a single scattering with oxygen reach the detector at energies above 12.35 MeV and are excluded from use in the SENT technique as indicated earlier.) The contribution of multiple scattering to the energy range [12.35,3.5] MeV, utilized in the SENT technique, is estimated from the Monte Carlo simulation by observing the weight of neutrons as recorded prior to their scattering in the test section; given that a source neutron has a weight of one. Table 2 shows the weight of rescattered neutrons relative to the total weight of scattered neutrons, noting that first collision neutrons prior to scattering have an energy equal to the source energy. The table shows that the rescattering weight is generally low and tends to increase at high energies, because of first collisions with oxygen, and at low energies, because of multiple scatterings with hydrogen. Since not all rescattered neutrons succeed in reaching the detectors because of their diverse angular distribution, the relative contribution of multiple scattering to the detector fluences is expected to be less than the relative weights of table 2. This argument is further supported by the fact that the SSM was able to predict the detector fluences reasonably well within the error band of the Monte Carlo results. Even if one conservatively takes the maximum deviation between the SSM results and the corresponding Monte Carlo results as the contribution of multiple scattering, this would not be more than 5%, considering the more accurate 8 × 8 mesh results of table 1.

The above analysis was considered for a 100-mm diameter test section completely filled with water. For water fractions less than unity for this test section or for smaller diameter test sections, one can expect the contribution of multiple scattering to be less than 5%, since less water is present. The analysis was considered for a flow at atmospheric pressure and at room temperature. At higher pressures the liquid density increases slightly, while at higher temperatures the neutron microscopic cross-section does not significantly change in the few MeV energy range in which the SENT technique is applied. Therefore, pressure and temperature may slightly affect the microscopic cross-section and consequently the scattering process, but this can be accounted for by adjusting the neutron cross-sections.

In conclusion, for test sections of 100-mm diameter or less, the SSM is adequate since the contribution of multiple scattering to the detector responses is small and can be ignored. For test section diameters more than 100 mm, the contribution of multiple scattering becomes more significant as the diameter increases. However, by collimating the scattered neutrons on their arrival to the detector, the contribution of multiple scattering can be reduced, since multiscattered neutrons reach the detector at angles different from that of single-scattered neutrons. Also, introducing corrections to the SSM to account for the effect of multiple scattering would be helpful. Therefore, the SENT technique potentially can be extended for application to larger test sections.

3.3.2 *Homogenization.* As discussed earlier, the detector response in the SSM is calculated by summing the contributions of individual fictitious cells constructed in the test section. Inside each cell, an averaged density is used in the calculations. This average density is obtained by assuming that the material inside the cell is uniformly distributed, or in other

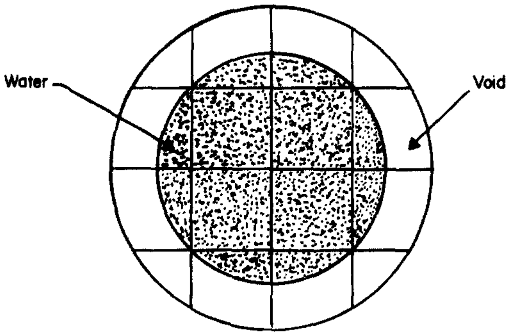

Figure 5. Inverted annular density distribution.

words by homogenizing the material inside the cell. Therefore, one can expect that the smaller the cell size, the closer the average density to the actual density and consequently the more accurate the SSM. In order to study the effect of this homogenization process, let us consider the inverted annular density distribution of figure 5. One can see that if a 4 × 4 mesh is constructed over the test section, some cells would be partially filled by water (to roughly ⅓ of their volume in this example). Homogenizing the liquid and the void in these cells to produce a mixture of equivalent density would fill the void volume with the mixture while reducing the density in the liquid volume. Then, the void volume would act as a scattering medium while the amount of scattering in the liquid volume would be reduced because of the density reduction. Therefore, using the SSM for this mesh structure would result in some error. By refining this mesh structure the magnitude of error can be reduced.

Table 3. Monte Carlo and single scattering model fluences for the inverted annular distribution of figure 4

Detector Number	MeV Scattering Energy Interval	10^6 x Fluence (Neutrons/cm^2/source neutron)		
		Monte Carlo	4 x 4 Mesh	8 x 8 Mesh
1	10.5 - 8.2	21.563 (5.17)*	20.23 (6.18)+	20.15 (6.55)+
2	10.5 - 8.2	18.462 (5.65)	16.46 (10.84)	17.28 (6.4)
3	10.5 - 8.2	4.822 (10.0)	7.532 (52.47)	13.09 (3.49)
1	8.2 - 5.8	13.271 (6.25)	17.40 (31.11)	13.35 (0.60)
2	8.2 - 5.8	33.929 (3.9)	33.14 (2.33)	34.00 (0.21)
3	8.2 - 5.8	27.537 (4.5)	26.32 (4.42)	27.28 (0.93)
4	8.2 - 5.8	9.126 (7.4)	11.19 (21.84)	8.232 (9.8)
2	5.8 - 3.5	10.55 (7.0)	16.38 (55.26)	11.90 (12.80)
3	5.8 - 3.5	28.26 (5.0)	29.07 (2.807)	30.42 (7.64)
4	5.8 - 3.5	24.839 (4.4)	23.70 (4.59)	24.08 (3.06)

* Fractional standard deviation (%)

\+ Fractional error relative to Monte Carlo (%)

Table 3 shows the SSM results for a 4 × 4 mesh and the finer 8 × 8 mesh, compared to those of the Monte Carlo method. The improvement in the SSM results introduced by refining the mesh structure is clear. However, in order to determine the water fraction in the cells of an 8 × 8 mesh, one would need at least 64 measurements, versus only 16 for a 4 × 4 mesh. Therefore, to improve the resolution of the SENT technique, one has to increase the number of measurements by the same order of magnitude as the desired improvement in resolution. One can notice that the effect of the mesh size on the SSM results is not as significant for the example of table 1 as that for the inverted annular flow regime of table 3. This is because the homogenization process in the "full of water" case has no effect, since the cells already are just filled with water with no void. The only improvement that would result by reducing the cell size in the full of water case would be due to the more accurate determination of the location of the scattering centers. Since the distribution of the material inside each cell would not be known, when the SENT technique is applied, it is desirable to use a fine mesh structure. The effect of using a coarse mesh on the reconstructed phase distribution is discussed in section 6.

4. NUMERICAL ANALYSIS

In section 2 the mathematical method for solving the SENT problem was discussed emphasizing the importance of constructing the direct mapping. The SSM, as shown above, provides an adequate direct mapping for the SENT problem. This makes it possible to implement the solution methodology of section 2 into a numerical algorithm. In this section this algorithm is developed, first for the ideal inverse problem where exact "error-free" measurements are assumed to be available, then for the applied inverse problem where statistical measurement errors are involved. The ideal inverse problem is used for testing the algorithm. Success in solving the ideal inverse problem does not necessarily guarantee a solution of the applied inverse problem. However, it provides insight into the nature of the inverse mapping involved and that could be helpful in solving the applied inverse problem.

4.1 *The successive approximation process*

In an ideal inverse problem, one can expect to find a mapping $\mathbf{m}^{-1}$ that exactly inverts the forward mapping $\mathbf{m}$; i.e., it satisfies the identify

$$\mathbf{m}(\mathbf{m}^{-1}\mathrm{S}) = \mathrm{S}, \qquad [16]$$

for all admissible data S. Uniqueness would require that

$$\mathbf{m}^{-1}(\mathbf{m}\rho) = \rho, \qquad [17]$$

for all admissible water fraction vectors ρ. The exact solution of the inverse problem is then given by

$$\rho = \mathbf{m}^{-1}\mathrm{S}. \qquad [18]$$

Since the direct mapping for the SENT problem is represented by the matrix $\mathbf{A}$ whose elements are defined by [15], the inverse mapping is the inverse matrix $\mathbf{A}^{-1}$. However, as clearly shown by relationships [15], one has to know the value of the vector ρ, in order to construct the matrix $\mathbf{A}$. In other words, in order to solve the SENT inverse problem, to find ρ, one has to known in advance the value of ρ so that the required inverse mapping can be constructed!

To overcome this problem, one can adopt the successive approximation process (SAP). In this method, an approximation of the value of ρ is provided and used to construct an "approximate" direct mapping $\mathbf{A}$ which is then inverted to obtain $\mathbf{A}^{-1}$. The resulting "approximate" inverse mapping maps the "results" vector S into a new solution ρ, which is used in turn to construct a new approximation for $\mathbf{A}^{-1}$, and so on.

The SAP is represented by

$$\rho_{k+1} = \mathbf{A}^{-1}(\rho_k)\mathrm{S}, \quad k = 0,1,2,\ldots, \qquad [19]$$

where k is the order of approximation and $\mathbf{A}^{-1}$ (ρ_k) indicates that the matrix $\mathbf{A}$ is constructed using the vector ρ_k. The natural next question would be that regarding the convergence and uniqueness of the solution.

The convergence of the SAP is examined in appendix A which shows that contraction mapping of relationship [19] within the closed interval [0,1] is essential for convergence. The mathematical conditions required for obtaining a contraction mapping are also discussed in the Appendix. If the SAP meets these conditions it will converge to a unique solution within the closed interval [0,1] according to the fixed point theorem, as shown in the Appendix. The numerical examples shown in section 6 demonstrate the success of the SAP in solving the error-free problem, provided that all the approximations of ρ are kept within the closed interval [0,1] in order to satisfy the SAP convergence requirements.

In the applied inverse problem the errors associated with the measurements make it difficult to keep the SAP within the [0,1] interval. However by applying the regularization process discussed in section 2, one would tend to bring the solution in any step of the SAP within the [0,1] interval. If after that the solution is still outside the [0,1] interval, one then should set the components of the solution that are greater than unity to unity and the negative ones to zero before starting the new SAP step. This is called the "adjustment" process and it ensures that the SAP maps the problem into the required closed interval [0,1]. One then has to test for the contraction of the SAP. If the SAP displays a contraction mapping then, as shown in appendix A, the problem will converge to a unique solution within [0,1]. Failure to obtain a contraction mapping within [0,1] would indicate either the solution exists outside the [0,1] interval or that an excessive regularization has been used such that the contraction nature of the mapping is destroyed. The former problem is usually encountered, as will be shown in section 6, when the solution exists close to the boundaries of the [0,1] interval (i.e. when a "full of water" problem is encountered). Here, because of the error in the measurements, the quasisolution of the problem might be a little off the boundaries of the interval and attempts to contain a solution within the [0,1] interval usually fail. The near-linear approach discussed later can be used in such circumstances to reach the solution. Excessive regularization, by using a very large value of the regularization parameter, would produce solutions within a smaller subinterval of [0,1]. If the solution exists outside this subinterval, the SAP would not be able to reach it and a noncontraction mapping would result. A loose regularization, on the other hand, would produce solutions outside [0,1] but by applying the cut-off process one restarts the new SAP with a solution within [0,1]. However, this may require more iterations until the SAP is reasonably self contained within [0,1], then the problem could be expected to converge to its unique solution.

One should mention that because of the errors in the measurements the quasisolution of the problem might contain components that are slightly off the [0,1] interval. This is tolerated by accepting a reasonable cut-off range, i.e. a reasonable margin outside [0,1]. A better quality of measurements or a larger number of measurements would result in a quasisolution that is closer to the exact solution.

4.2 *Physical conditions for contraction mapping*

In order to be able to solve the nonlinear SENT problem, it is required that the SAP meets the conditions of contraction mapping outlined in appendix A. These conditions are

$$0 \leqq \beta \leqq \alpha < 1, \qquad [20]$$

where α is a positive number and β is the maximum distance in mean-free paths a neutron travels in any cell of the constructed mesh. Here, these conditions are examined in order to find their physical implications.

The maximum distance (in units of mean-free path) a neutron travels in a given cell is that which it travels after scattering. This is because the neutron loses energy in the scattering process, and consequently its mean-free path decreases. Also, for a well collimated incident beam, scattered neutrons cross the cells in directions inclined with the cell edges, resulting in longer travel distances as compared to those of source neutrons. Therefore, the maximum distance a neutron travels in cell j is

$$\beta_j = \max_i \Sigma_i d_j / \sin \theta_i, \quad i = 1, \ldots, M,$$

where β_j is in mean-free paths, Σ_i is the cross-section of a neutron contributing to the detector response S_i, d_j is the maximum width of the cell j, and θ_i is the scattering angle corresponding to S_i. The maximum cell width for a square mesh as that in figure 3 is encountered for cells that lie on the diameter of the test section, and is equal to $DN^{-1/2}$, where N is the total number of cells and D is the diameter. Therefore, one can write

$$\beta = \max_j \beta_j = (DN^{-1/2}) \max_i \Sigma_i / \sin \theta_i.$$

Each detector response corresponds to a particular energy E_i uniquely related to the angle θ_i according to [11]. Further, only scattering by hydrogen is recorded, resulting in $E_i = E_0 \cos^2 \theta_i$, where E_0 is the energy of the incident neutron. Therefore,

$$\beta = (DN^{-1/2} E_0) \max_i \Sigma_i / (E_0^2 - E_i^2)^{1/2} = \max_i \beta_i. \qquad [21]$$

Figure 6 shows the variation of β_i with energy, for the detection energy range used in the SENT problem, with the upper energy being $(15/17)E_0$, and the lowest energy being $(1/4)E_0$. In the figure a 4×4 ($N = 16$) mesh constructed in a 100-mm diameter test section was used. One can see that β is always less than unity with tendency to increase at both high and low energy. This gives another good reason to exclude high and low detection energies from the information utilized in the SENT technique. Note that for test sections smaller

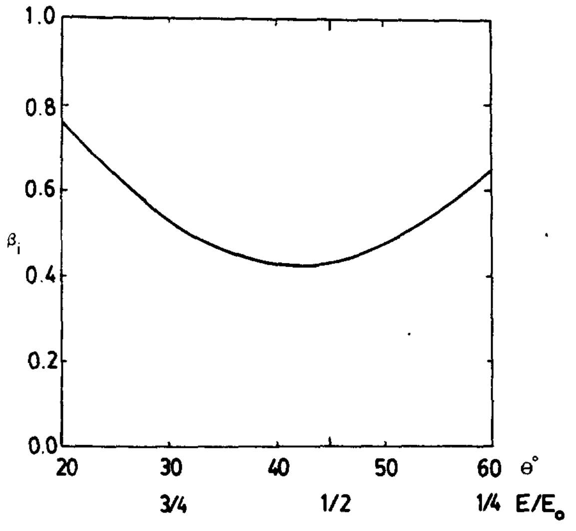

Figure 6. Scattering distance in cell i, β_i, in mean-free paths vs scattering energy or angle.

than 100 mm in diameter and for mesh structures finer than the 4 × 4 mesh, the value of β as indicated by [22] would be less than that shown in figure 6.

One can conclude that, provided a reasonably fine mesh structure is used and the high- and low-energy neutrons are excluded, the contraction mapping requirements can be met in the SENT technique. Practical applications usually require fine mesh structures, while high detection energies are excluded to avoid oxygen scatterings and low energies are excluded to reduce the effect of multiple scattering. Therefore, the contraction mapping requirements do not impose additional restrictions to those required by other practical and physical considerations.

4.3 *Near-linear problem*

Because of the exponentional nature of the matrix **A**, the matrix does not significantly change at the last stages of the SAP, where the problem is close to its final solution. In this case, one can consider the problem to be nearly linear and can turn to noninversion techniques for solving linear problems. This reduces the computational effort spent in the matrix inversion process. Noninversion techniques, such as the Bayesian method discussed by Hussein *et al.* (1983), adjust the solution iteratively by introducing appropriate correction factors and are widely used in conventional attenuation tomography where large matrices are encountered. In addition to computational savings, noninversion methods can be utilized when the inversion method does not result in a contraction mapping near the [0,1] boundaries. Since noninversion methods introduce slight corrections to the previous solution approximation, they are useful in guiding the SAP towards the near boundary solution without sharply bringing the solution outside [0,1]. It is not desirable to use noninversion methods all the way through the SAP in other cases. This is because the small changes introduced to the solution would require a large number of iterations.

4.4 *Numerical algorithm*

Figure 7 shows a flow chart outlining a numerical algorithm for solving the SENT inverse problem by implementing the abstract aspects discussed in the previous sections. The nonlinear problem is addressed through the successive approximation process (SAP) initiated by the zeroth approximation (initial guess). Once a solution approximation is available, the direct mapping (matrix **A**) is constructed using the single scattering model, as shown in section 3. This enables solving the direct problem and calculating the detector responses corresponding to the given solution approximation. The calculated results are then compared to the measured ones and a decision is made on whether the given approximation is an acceptable solution of the problem. The acceptability of the solution is determined by monitoring four norms that measure the difference between the calculation and measurements, the convergence of the SAP and the deviation of the constructed solution approximation from both the upper and lower bounds of the interval [0,1]. If the solution is acceptable, then the error associated with the solution is estimated and the problem is terminated. Otherwise, the near-linearity of the problem is checked by monitoring a norm that provides a measure of the difference in the constructed direct mappings between any two successive approximations. If near-linearity is not achieved, the inverse mapping is constructed using a regularized least-squares inversion, as discussed in section 2. Then a new solution approximation is obtained. When near-linearity is reached, a Bayesian algorithm is used to obtain a new solution approximation. The Bayesian method, as discussed by Hussein *et al.* (1983), introduces a probabilistic correction to the given solution approximation, without explicitly constructing the inverse mapping. The new solution approximation obtained is examined and the two norms measuring the deviation from the upper and lower bounds of the interval [0,1] are calculated. Then, the solution is adjusted such that all its elements lie within the interval [0,1], in order to guide the solution for convergence within this interval. At the moment,

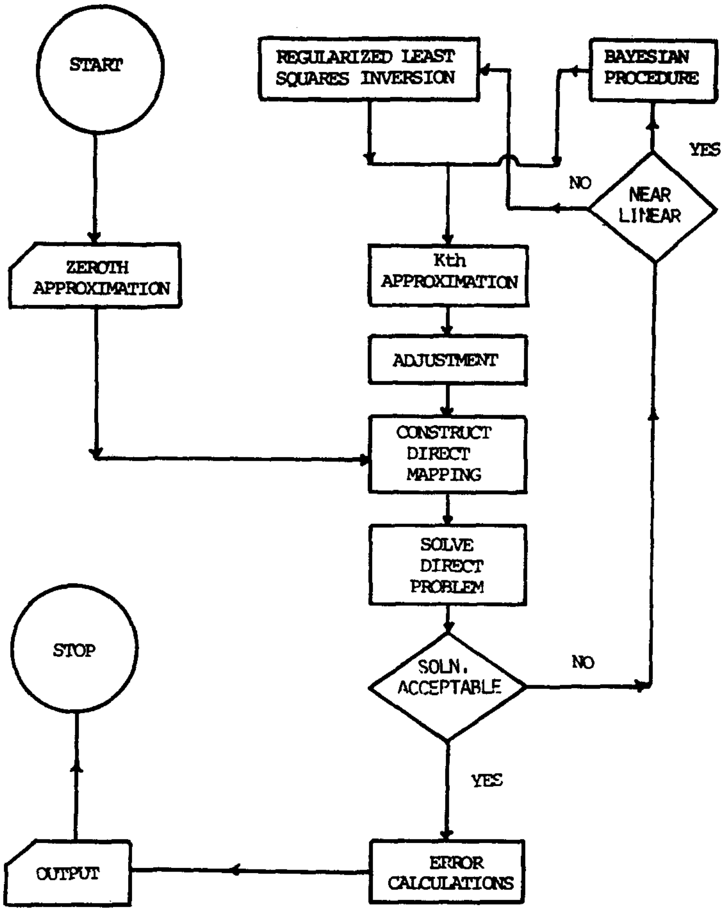

Figure 7. Flowchart of the computational procedure.

simple adjustment is done by setting all negative elements of the solution to zero and those larger than unity to one; however, a more sophisticated approach is possible. The adjusted approximation is then used to repeat the successive approximation process.

5. EXPERIMENTAL DESIGN

A detailed design of an experimental setup for the SENT technique is reported by Hussein *et al.* (1984). This setup meets the requirements imposed on the SENT technique by the physical and mathematical considerations discussed in the previous sections. The design discussed is by no means the only one possible and can be altered in many ways. No attempt is made here to repeat the details of this design. However, the design parameters are discussed in view of the SENT requirements, indicating the various choices available. This would enable a potential user of the SENT technique to design the system to meet the available resources and minimize costs. The choice of the neutron source, detection system and associated electronics are now discussed.

5.1 *Neutron source*

In the analysis presented in section 3, a single well-collimated beam of 14-MeV neutrons was assumed. This was done mainly to simplify the analysis. Here the effect of energy, angular distribution, geometry and intensity profile of the neutron source are examined.

A monoenergetic 14-MeV source was used in the present work. However, it is possible, at least in principle, to use a source of different energy. The only restriction is that the diameter of the test section used is of the same order of magnitude as the mean-free path of the source neutron, in order to reduce the effect of multiple scattering. One may be able to use a multienergetic source of known energy spectrum. However, special attention must be paid to excluding oxygen scattering and modifying the single scattering model to account for source neutrons of different energies. Since many multienergetic neutron sources are available, an effort should be made to tailor the SENT technique to accommodate these sources.

The angular distribution of the neutron source directly affects the SENT technique since the energy-angle relationship of scattering is utilized. If the angular distribution is known, it can be easily accommodated by tailoring the single scattering model. Therefore, in principle, an isotropic source can be utilized provided that attention is given to eliminating neutron incidence on layers above and below the tomographic section, for example by appropriate shielding of the source, test section, or detectors. In choosing the geometry of the neutron source one has to ensure that the source is wide enough to cover the whole tomographic section, as shown in figure 4, in order to enable neutrons to reach each cell.

Although a uniform beam profile is assumed in the present work, the variation of the profile can be easily accommodated in the single scattering model through the W_j weighting term in [15]. However, the intensity distribution of the incident beam can be measured and incorporated into the analysis.

5.2 *Neutron detector*

The desired characteristics of the neutron detector to be used in the SENT technique are basically (1) capability to measure the energy spectrum whose components are required for solving the inverse problem, (2) small size in order to easily relate the energy to angle of scattering and (3) insensitivity to gamma-rays that almost always accompany neutron production. Organic scintillation detectors have these characteristics. They are capable of measuring the energy spectrum with a relatively high efficiency even for small detectors, and they generally have pulse shape characteristics that enable discrimination against gamma-rays. The favoured organic scintillator has been NE-213 (made by Nuclear Enterprises Ltd.), a xylene-based liquid that exhibits good pulse shape discrimination (PSD) properties. NE-213 has an enhanced emission of delayed light which gives its good PSD characteristics. Since it is noncrystalline, NE-213 is isotropic in response to neutrons and is not sensitive to mechanical or thermal shocks. An NE-213 detector is inexpensive and can be easily constructed in the laboratory. A miniature detector (12.5-mm diameter and 12.5-mm length) was used in the present work.

5.3 *Electronics and discrimination against gamma-rays*

The main purpose of the electronic circuit associated with the detector is to provide a pulse-height distribution from which the energy spectrum can be deduced. This is usually obtained by utilizing a multichannel analyzer with the channel number calibrated to provide the energy information. Also, a very effective discrimination electronic circuit is required to eliminate gamma-ray pulses from the desired neutron-pulse-height distribution. A zero-crossover-timing circuit similar to that of Perkins & Scott (1979) is used in the SENT technique.

5.4 *Unfolding of neutron spectrum*

The pulse-height distribution produced by the detector is not directly related to the neutron energy spectrum. In organic scintillators, neutrons give rise to recoil protons which in turn cause the scintillation process. In general, there are two approaches to unfolding the neutron spectrum, namely, the differential and the response matrix approaches. Differential methods depend on the ideal rectangular response function of recoil protons to monoenergetic neutrons. A computer code has been developed by Toms (1971) using the differential approach and utilizing a nonlinear correlation for relating the pulse-height distribution to the proton distribution. Differential methods are only suitable for small detectors where the rectangular response function is not significantly altered by the contribution of neutron multiple scattering. On the other hand, in the matrix response approach, a response matrix is constructed for the detector used. The response matrix can be either measured or calculated using the Monte Carlo method. A matrix inversion unfolding computer code such as the FORIST code (1975) can be used to obtain the neutron energy spectrum.

Matrix inversion methods are more elaborate and require more computational effort as compared to differential methods. For the small detector used in the SENT technique, a differential method seems to be suitable, provided that appropriate correlations are used for relating the light output to the proton distribution and for accounting for the wall effect (neutron escape).

5.5 *Experimental results*

In the experiments presented in detail by Hussein *et al.* (1984), a 14-MeV continuous source produced by the ^3H (^2H, *n*) reaction in a small low-voltage accelerator was employed. An iron collimator of 350-mm effective length was used, resulting in a neutron flux of 1.8 × 10^6 n/cm^2/s incident on the test section located at the end of the collimator. Three full of water test sections of 12.7-, 23.9- and 46.8-mm diameters were located at the end of the collimator and the fluences of the scattered neutrons at different positions were recorded. Details of these measurements can be found elsewhere (Hussein 1983; Hussein *et al.* 1984). Here, only some of the results are presented in order to demonstrate how the measurements required by the SENT technique can be obtained experimentally.

The energy spectrum of the incident beam was measured by locating the detector at the end of the collimator. The purpose of this measurement, in addition to measuring the source strength, was to confirm the capability of the detection system to reproduce the known source energy spectrum. The results of this measurement are presented in figure 8 and were obtained by unfolding the spectrum from the pulse-height distribution using a differential

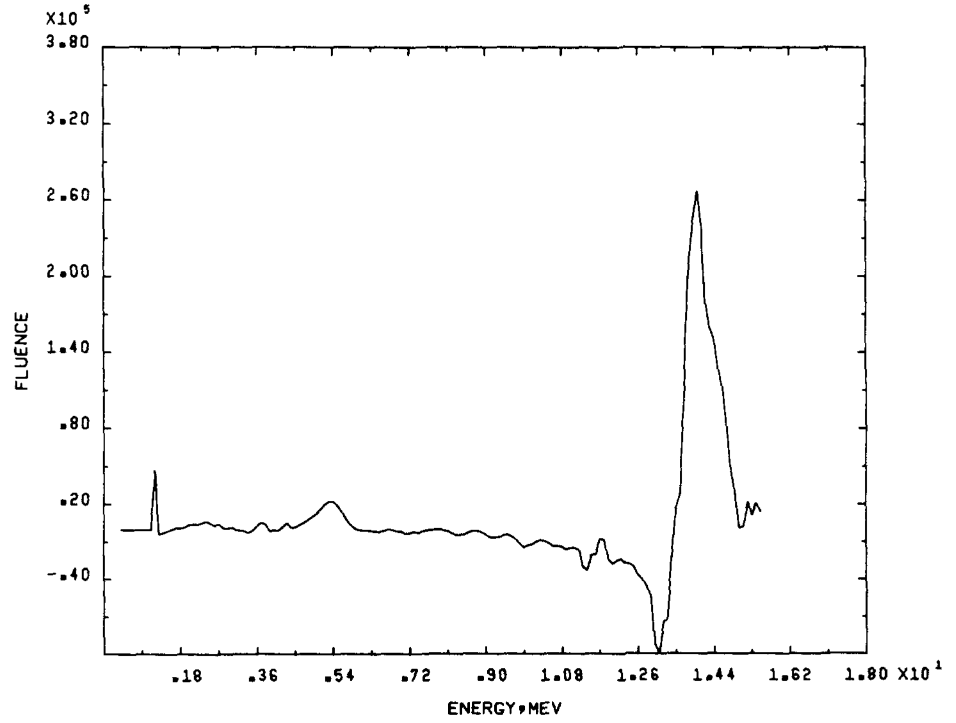

Figure 8. Unfolded 14-MeV neutron source spectrum.

method similar to that of Toms (1971). The spectrum depicts clearly the 14-MeV expected peak, indicating that the neutron spectrum is not significantly softened by the collimator (large energy softening would results in a wider peak). Two defects are observed in figure 8, namely, the negative flux below the 14-MeV peak and a small peak at 1.2 MeV. The negative flux is due to the anisotropy above 10 MeV of neutron scattering by protons in the detector, which distorts the rectangular response function of the detector. Therefore, neutrons of energy above 10 MeV were not considered for use in the SENT technique, since no correction was made to account for the anisotropy in the unfolding method. Results below 2 MeV, as indicated by Toms (1971), are not considered to be reliable when a differential unfolding method is used, since carbon and inelastic scattering in the detector are not accounted for in the method. Therefore, the small peak at 1.2 MeV is not real and should be ignored. Therefore, the results of figure 8 were considered to be successful since the 14-MeV peak was clearly observed, and the source strength obtained from them was comparable to the expected one, as discussed by Hussein *et al.* (1984).

Given the success of the direct measurement of the energy spectrum of the neutron beam, the detector was used to measure the spectrum of the neutrons scattered by each of the three test sections. The detector was located at different positions surrounding the test section and downstream of the neutron beam, in order to provide a sufficient number of results that could be utilized in the SENT technique. The details of these measurements are reported by Hussein *et al.* (1984); however, figure 9 shows the energy spectra obtained for the three test sections at a specific location as compared to those calculated using a Monte Carlo simulation of the experiment. The results of the experiments strongly reflect the trend shown by the calculations; however, there is some discrepancy between the two when the numerical values are compared. These numerical values are important if the measurements are to be used in the SENT technique, since they strongly reflect the amount of the material present.

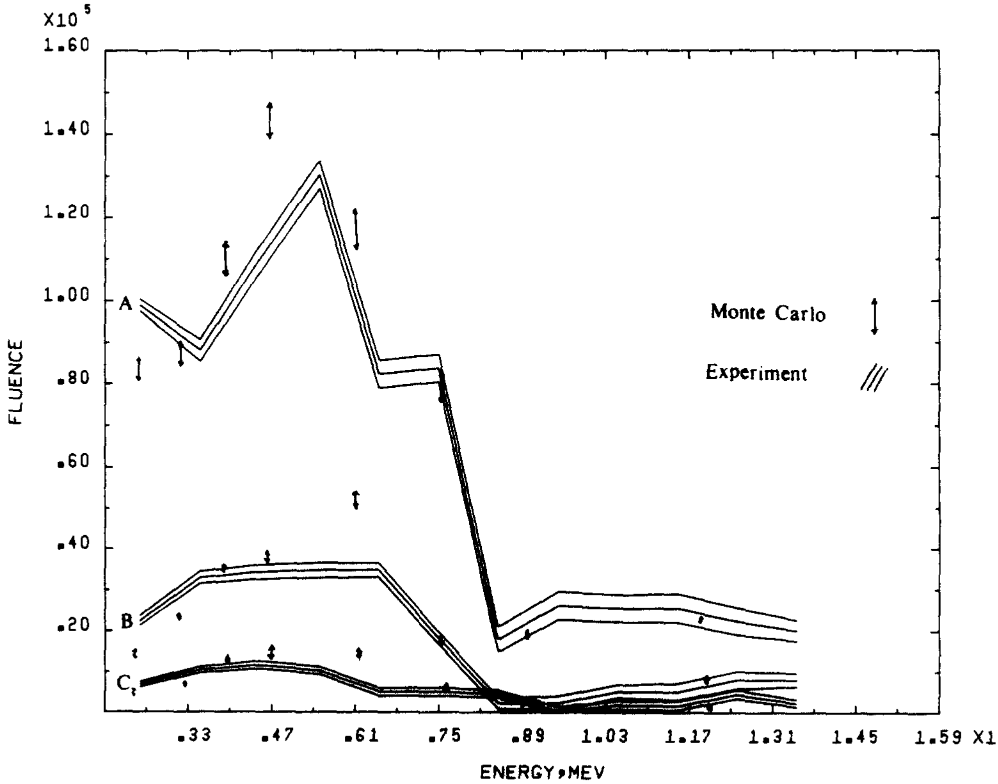

Figure 9. Comparison between experimental and Monte Carlo results for test sections *A*, *B* and *C* of diameters: 46.8, 23.9 and 12.7 mm, respectively.

The numerical discrepancy is thought to be mainly due to the possible errors in the correlations used in the differential method to relate the light output to the proton distribution and the latter to the neutron distribution, since they were developed for larger detectors. Further effort must be made to refine these correlations before utilizing the differential method to provide the detector responses used in the SENT technique. The more reliable response-matrix methods may also be used, if the computer resources required by these methods are available.

One can conclude from the experimental results presented above that, although further refinement of the detection system is required, the system is capable of providing the measurements needed by the SENT technique. The detection system is relatively simple and has been widely used in many applications; therefore, the experimental requirements of the SENT technique can be met in practical situations.

6. RECONSTRUCTION OF PHASE DISTRIBUTION

The algorithm developed in section 4 is applied to reconstruct the phase distribution for different flow regimes utilizing results of the SSM, Monte Carlo simulations and the experiments. The SSM results are considered to be error-free, except for round-off error, since the SSM is exactly the model used in the reconstruction process. Therefore, one would expect to exactly reconstruct the phase distribution, when the SSM results are utilized. On the other hand, both Monte Carlo and experimental results contain the contribution of multiple scattering and statistical errors. Also, the experimental results contain the errors introduced by the detection system, mainly unfolding errors. The effect of these different errors on the reconstruction process is examined in the following examples where different phase distributions are considered. In the following examples, unless otherwise specified, a 100-mm diameter test section with a 4 × 4 rectangular mesh is considered, and 20 detector responses (measurements) are utilized and obtained using eight detectors arranged as shown in figure 4. In all examples, the phase distribution is presented such that the neutron beam is incident from the left-hand side of the test section, as is the case in figure 4.

6.1 *Annular distribution*

Figure 10(A) shows the original density (water fraction) of the annular water distribution to be reconstructed, while figures 10(B) and 10(C) show the reconstructed phase distribution utilizing the SSM error-free results and those of the Monte Carlo simulation, respectively. The reconstructed distributions were obtained after the successive approximation process (SAP) converged within a distance less than 10^{-4}, defined using an Euclidean norm, see Hussein *et al.* (1983). Similar definitions were used for the norm $\| \cdot > 1 \|$ that provides a measure of the deviation of the solution from the upper bound of the interval [0, 1] and the norm $\| \cdot < 0 \|$ that measures the deviation from the lower bound of the interval. The deviation between the measured and calculated detector responses is defined by the Euclidean norm $\| S - S^c \|$, given in the figures relative to the Euclidean norm $\| S \|$ of the measurement vector.

Figure 10(B) shows that the phase distribution is almost exactly reconstructed from the error-free results, as one would expect, indicating the success of the numerical algorithm in solving this ideal inverse problem. The small errors associated with the results are round-off errors, and the $\| \cdot > 1 \|$ and $\| \cdot < 0 \|$ norms indicate that the solution is kept inside the [0, 1] interval with a very small round-off error.

The phase distribution reconstructed from the Monte Carlo results and shown in figure 10(C) successfully depicts the void zone in the original distribution. However, deviation from the original density is observed in the cells that were partially filled. This is mainly because of the homogenization of the phases that results in shifting the center of scattering (position of average neutron scattering) and consequent adjustment of the cell's density to reproduce the

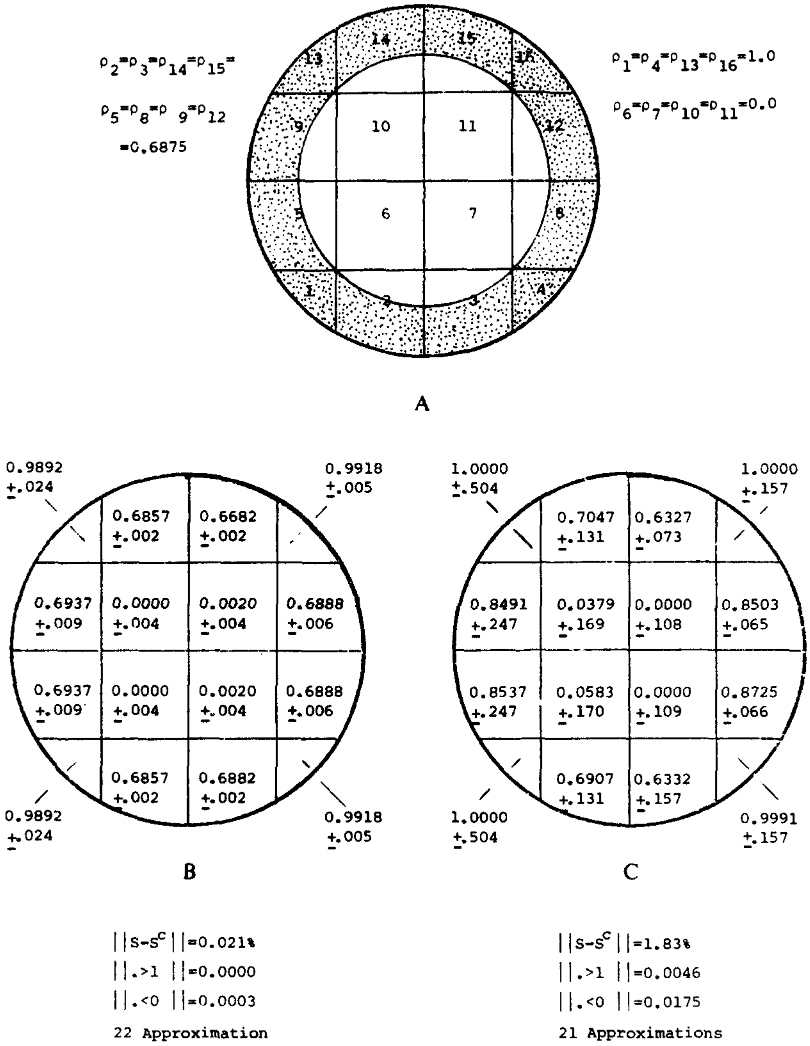

Figure 10. Reconstruction of annular density distribution. (A) Original water-fraction distribution, (ρ_i), (B) reconstructed distribution from error-free results, and (C) reconstructed distribution from Monte Carlo results.

scattering fluences recorded by the detector. This was not observed in the error-free results, since these results were produced using the SSM with the cells originally being homogenized.

The unusually high error associated with the two edge cells closer to the neutron beam is due to the fact that these cells are heavily screened from the detectors by many other cells, and consequently suffer from the accumulation of errors in the screening cells.

One can expect a significant improvement in the reconstructed density if the homogenization effect is reduced by using a finer mesh structure. No attempt was made to reconstruct the phase density distribution in a finer mesh using Monte Carlo results because of the large computer cost involved in producing the required large number of detector responses. However, even for the coarse mesh structure of figure 10, the reconstructed density distribution depicts the original phase distribution within a reasonable error range.

6.2 *Inverted annular distribution*

Figure 11 shows the original and the reconstructed phase distributions. Again, one can see the expected success of the error-free case. The Monte Carlo reconstructed distribution is different from the original one because of the homogenization process. It is interesting to

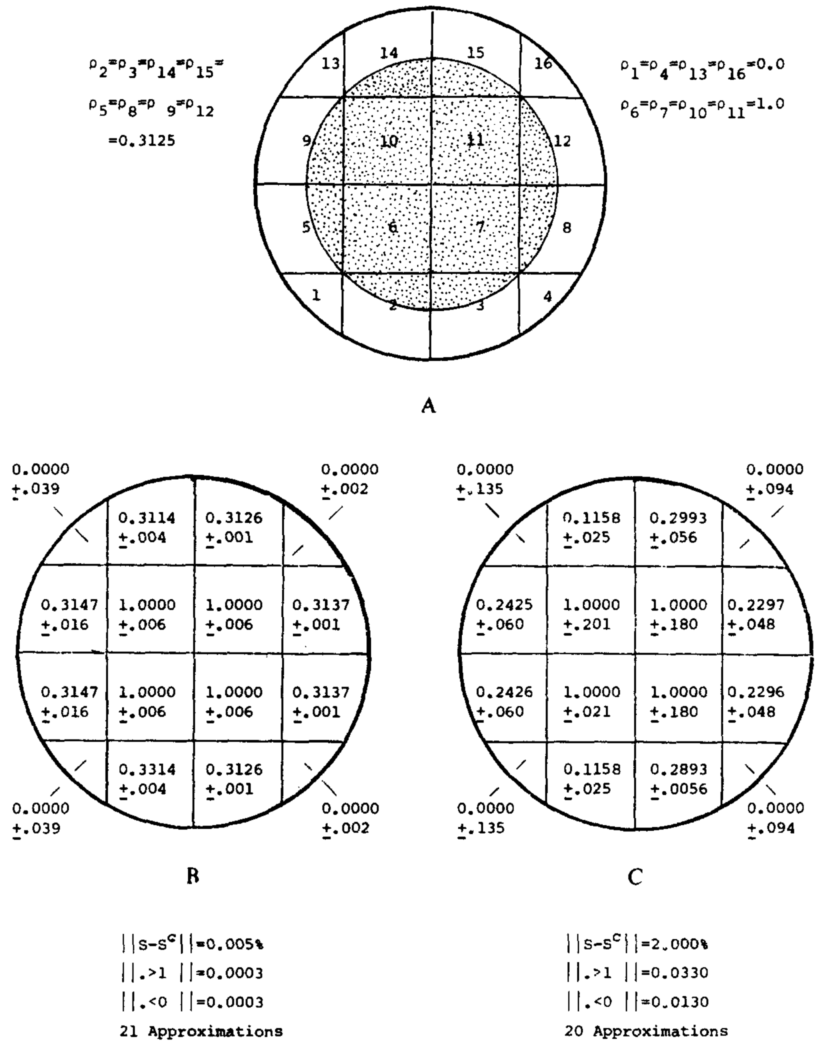

Figure 11. Reconstruction of inverted annular density distribution. (A) Original water-fraction distribution, (ρ_i), (B) reconstructed distribution from error-free results and (C) reconstructed distribution from Monte Carlo results.

note, in figures 10(C) and 11(C), that while homogenization tends to inflate the density in the annular distribution, it tends to reduce the density in the corresponding cells in the inverted annular distribution. This is because the two distributions complement each other and one could expect the homogenization process to have opposite effects in the two cases.

6.3 *Stratified distribution*

The original stratified distribution considered is shown in figure 12(A) and the reconstructed distributions for the error-free and the Monte Carlo cases are shown in figures 12(B) and 12(C), respectively. As expected, the ideal inverse problem is successfully solved. However, the distribution reconstructed from the Monte Carlo results underestimates the density distribution in the stratified section while slightly increasing the density in the void section. This is due to neutron rescattering caused by the longer neutron path length encountered in this case. Rescattering tends to bring more neutrons to the detector and consequently increases the detector response. This increase can be interpreted by the reconstruction algorithm as either an increase in the water density to cause more scattering or a decrease in water density to lessen the neutron attenuation, since both result in an increase in the detector response. This could explain the density increase in the stratified

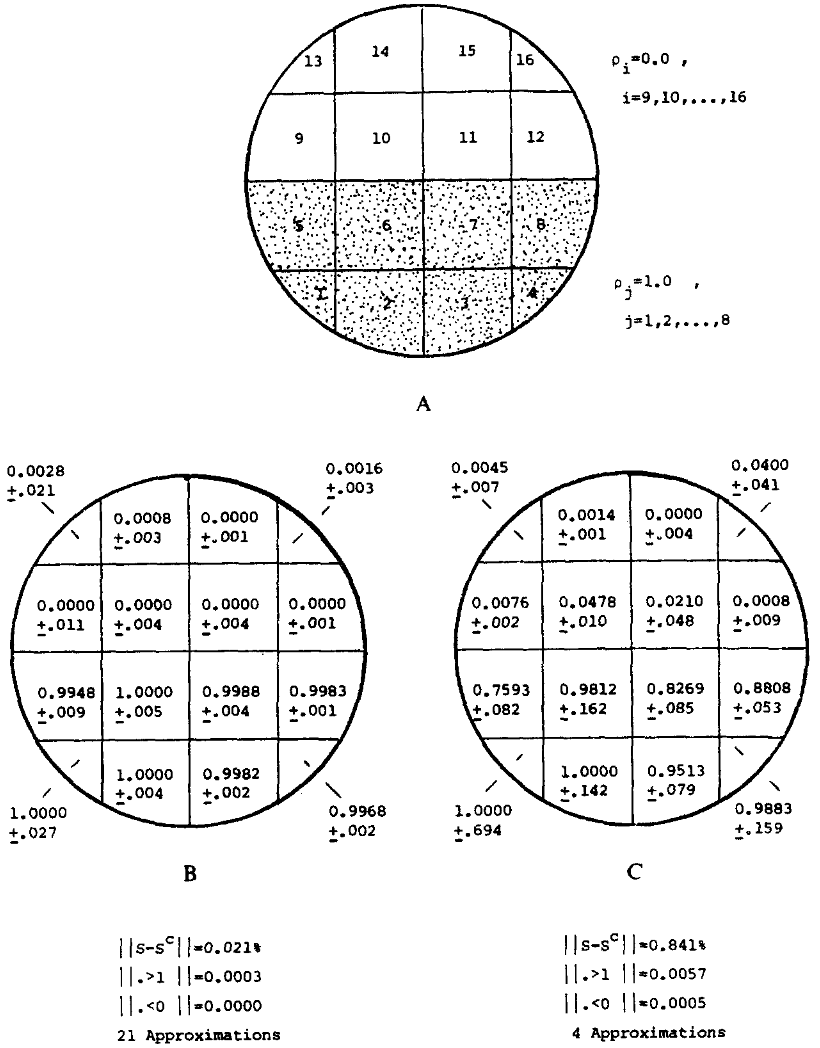

Figure 12. Reconstruction of stratified density distribution. (A) Original water-fraction distribution, (ρ_i), (B) reconstructed distribution from error-free results and (C) reconstructed distribution from Monte Carlo results.

section and the density decrease in the void section. Nevertheless, the stratification of the water phase is well depicted by the reconstructed distribution.

6.4 *Full of water test section*

The contribution of multiple-scattered neutrons in this case is larger than in any of the cases considered above, since the test section is of a diameter equivalent to one mean-free path of neutrons in water and is fully occupied by water. Also, this case challenges the numerical algorithm used in the reconstruction process, since it results in a solution on the upper bound of the [0, 1] interval, making it difficult for the successive approximation process to keep the solution within this interval to achieve convergence according to the requirements of Appendix A. This problem can be solved, as discussed in subsection 4.1, by using the Bayesian method, rather than the regularized least-squares inversion method. Because the former method introduces small gradual corrections to the given solution approximation, it is useful for use in the cases where the inversion method fails to keep the solution within the [0, 1] interval, as in the case encountered here.

Neutron rescattering, as explained before, results in either a reduction or an increase in the reconstructed density. This can be observed in the present case for the distribution

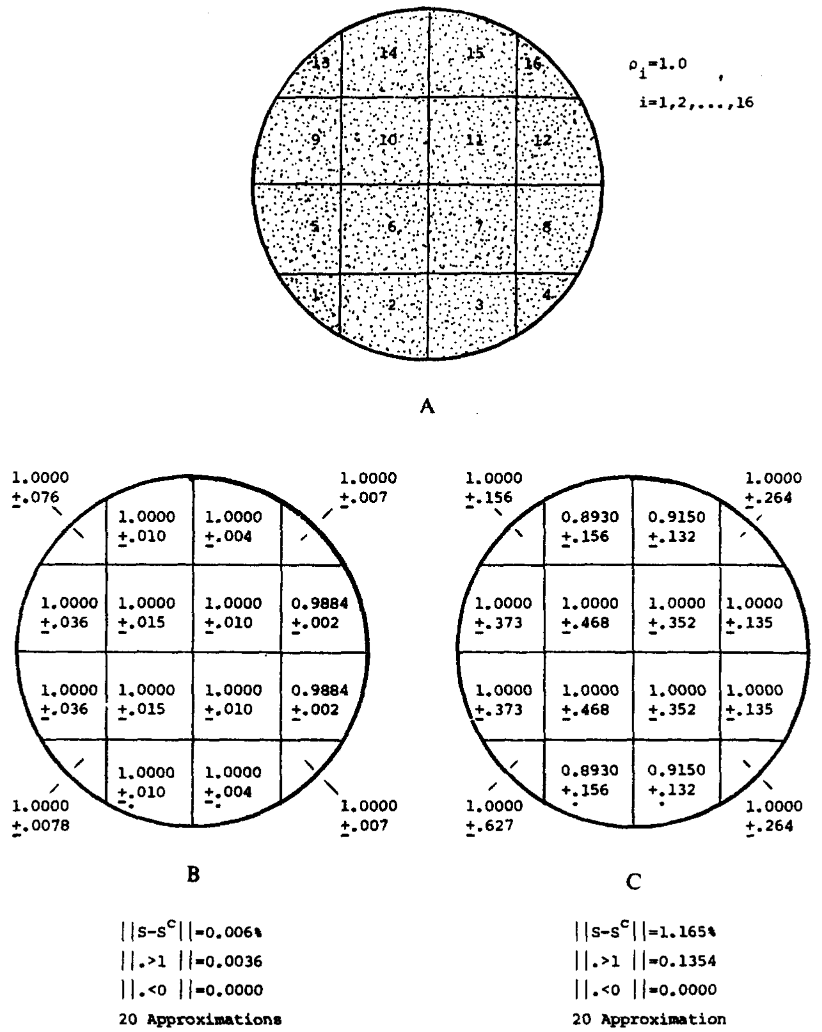

Figure 13. Reconstruction of "full of water" distribution. (A) Original water-fraction distribution, (ρ_i), (B) reconstructed distribution from error-free results and (C) reconstructed distribution from Monte Carlo results.

reconstructed from the Monte Carlo results shown in figure 13(C). While the density in some cells is lower than the original density, the $\| \cdot >1 \|$ norm has a value larger than that encountered in all the previous cases, indicating that the water fractions in many cells tend to exceed unity. However, the dominant presence of the water phase is depicted by the reconstructed phase distribution.

6.5 *Experimental results*

The detector responses measured experimentally for a full of water aluminum test section of 46.8-mm internal diameter 50.9-mm outside diameter are used in the present case to reconstruct its phase density distribution. The measurements were taken at four detector locations on one side of the test section resulting in 18 detector responses; after excluding low energies and high energies, in addition to those that correspond to angles of scattering from outside the test section. Figure 14 shows the reconstructed density distribution inside both a 4 × 4 and a 3 × 3 mesh. In both cases, the density was underestimated for the cells that are closer to both the detectors and the incident neutron beam. This could be explained by the fact that the contribution of these cells to the detectors is larger than other cells, and consequently these cells tend to carry the effect of the deviation of the measurements from

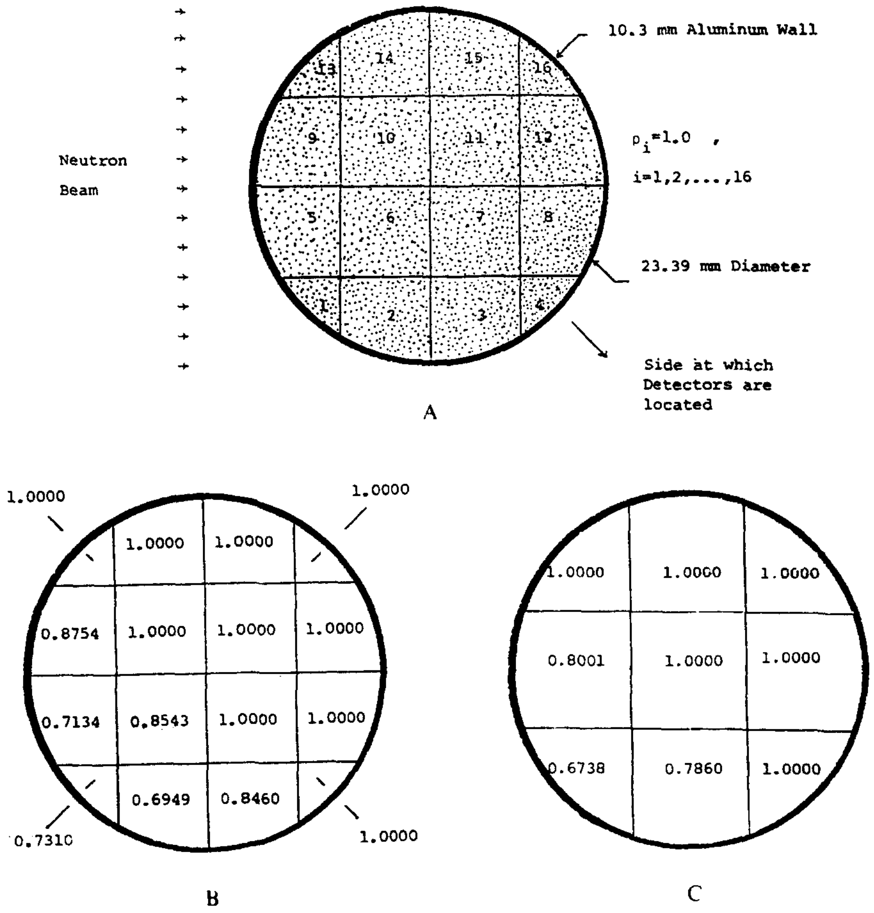

$||S-S^c||=5.515\%$
$||.>1||=0.0476$
$||.<0||=0.0000$
10 Approximations

$||S-S^c||=5.538\%$
$||.>1||=0.0606$
$||.<0||=0.0000$
10 Approximations

Figure 14. Density reconstruction from experimental results. (A) Original distribution, (B) reconstructed distribution for a 4 × 4 mesh and (C) reconstructed distribution for a 3 × 3 mesh.

the SSM results. In attempts to reduce the effect of this deviation, the overdetermination of the problem was increased by using the 18 detector responses to obtain the density in a 3 × 3 mesh. However, no significant improvement was observed in the reconstructed distribution, as figure 14(C) shows. This shows that the deviation is due to systematic errors inherent in the measurements, rather than statistical errors. As explained in subsection 5.5, errors in the correlations used in the unfolding procedure seem to be responsible for the deviation between the numerical values of the measurements and calculations. Therefore, further refinement of the unfolding procedure is expected to result in a significant improvement in the reconstructed density distribution. The asymmetry observed in the reconstructed distribution is due to the fact that the measurements were taken at one side of the test section and that the cells closer to the detector are more affected by measurement errors. Taking symmetrical measurements on both sides of the test section would result in a symmetrical distribution, but not necessarily a better one, unless the quality of the measurements themselves is improved.

It should be mentioned that other experimental parameters such as the nonperfect collimation of the neutron beam or the nonuniformity of its profile, or the use of a small detector, rather than a point detector, do not seem to have a significant effect on the reconstruction process, as discussed by Hussein (1983). One should also note that the aluminum wall of the test section has a small effect on the reconstruction process because of the low value of aluminum neutron cross-section at the energies considered and the small wall thickness used.

6.6 *Effect of regularization parameter*

As discussed in sections 2 and 4, the value of the regularization parameter τ^2, used in constructing the inverse mapping, has to be chosen such that it results in a reconstructed water fraction distribution closest to the actual distribution and lies reasonably well within the expected [0, 1] interval. In the examples presented above a value of τ^2 equal to N (number of unknowns) was used for problems utilizing either the Monte Carlo or the experimental results (no regularization is required for error-free problems). Here, the effect of the value of τ^2 on the solution is discussed.

The reconstruction of the annular distribution of figure 10 was done using different values of τ^2 and the results are summarized in table 4, with the norm $\| \rho^s - \rho^a \|$ being an Euclidean norm defining the difference between the actual water fraction vector ρ^a and the reconstructed one ρ^s, and the other three norms as previously defined. The table shows that the closest solution to the actual solution was obtained for $\tau^2 = 16$. This was also observed for other problems, as shown by Hussein (1983). The table also shows that the largest deviation from the [0, 1] interval, as the norms $\| \cdot <1 \|$ and $\| \cdot >1 \|$ indicate, tends to occur at small values of τ^2. This is because small values of τ^2 do not introduce enough regularization to contain the solution within the [0, 1] interval. Excessive regularization tends to preserve the nonnegativity of the solution; however, this is at the expense of further deviation from the actual solution and increasing departure from the unity upper limit, as table 4 shows. As explained by Hussein (1983), the value $\tau^2 = N$ allows the solution domain to expand up to its (weak) upper bound. Allowing the solution to exceed this upper bound by using a small value (of τ^2) is not reasonable, while limiting the expansion to values below the upper bound is a restrictive action. Therefore, it seems natural to choose the $\tau^2 = N$ value, as supported by the result of table 4. One last point: For all the τ^2 values, the successive approximation process converges, indicating that the conditions for contraction mapping are not affected and the fixed point theorem, upon which the method of solution is based, is still applicable.

7. SUMMARY AND CONCLUSIONS

In this paper, the fundamental aspects of solving the inverse problem of the SENT technique were discussed leading to a numerical algorithm for reconstructing the phase density distribution. The paper also discused the physical and experimental requirements of the technique and presented some numerical and experimental results to demonstrate the capabilities and limitations of the technique. The single scattering model, which is the workhorse of the reconstruction algorithm, was developed and compared to the more elaborate Monte Carlo simulations to investigate the effect of neutron multiple scattering and homogenization of the phases inside the fictitious cells constructed over the test section.

Table 4. Regularization of the problem of reconstructing the annular distribution of figure 10

NORM $/\tau^2$	0	4	8	16	32	64	128
$\|\rho^s-\rho^a\|$	0.1056	0.0936	0.0595	0.0332	0.0481	0.0655	0.0789
$\|s- s^c\|$	0.0277	0.0165	0.0183	0.0183	0.0191	0.0351	0.0598
$\|.>1\|$	0.0618	0.0307	0.0	0.0461	0.0411	0.0761	0.0724
$\|.<0\|$	0.1885	0.0456	0.0183	0.0175	0.0094	0.0	0.0

It was concluded that as long as the diameter of the test section is of the same order of magnitude as the mean-free path of source neutrons in water, the contribution of multiple scattering is not significant enough to invalidate the single scattering model. It was also shown that the homogenization effect can be reduced by using smaller cells. The experimental requirements of the SENT technique were shown to be within reach of the available neutron source and detector technology, and indeed most of the required techniques are being widely used.

While in this paper the theoretical and experimental fundamentals of the SENT technique were emphasized, more details are given by Hussein (1983). The method presented here, though developed particularly for neutron scattering is also applicable to gamma-ray scattering techniques as shown by Hussein & Kondic (1984).

Although it was indicated that some refinement of the unfolding procedure used to obtain the required neutron energy spectra is required, the SENT technique appears to be a valuable tool for obtaining the phase distribution in steam–water flow systems. The reconstructed distributions, presented here, showed the ability of the SENT technique to reasonably reproduce the phase distribution. To improve the unfolding procedure, correlations relating the detector light output to the corresponding proton and neutron distributions need refining to accommodate the miniature detector used in the SENT technique, since existing correlations were based on large detectors. Alternatively, one can generate the response matrix of the detector and use a matrix inversion method to unfold the neutron energy distribution. Although a 4 × 4 rectangular mesh structure was used for reconstructing the phase distribution, larger mesh structures can be used, as shown by Hussein (1983), and it is possible to tailor the technique to fit curved mesh structures.

The SENT technique is expected to perform well in high-temperature systems, particularly if a temperature correction is introduced to the neutron cross-sections. Since fast neutrons easily penetrate metallic pipes, and the effect of the metal can be incorporated into the single scattering model, the SENT technique is also suitable for high pressure systems. The SENT technique is also potentially applicable to transient system since only a single radiation exposure is required and neutron generators of high intensity are available. Given the fact that neutron interactions are nucleus-based, rather than electron-based as the case for photons, the SENT technique can be easily extended to various gas–liquid systems, and can be used for composition measurements, as suggested by Hussein (1984). In short, the single-exposure neutron tomography technique presented here is potentially a valuable tool for diagnosis of multiphase flow systems.

REFERENCES

BANERJEE, S. & CHAN, A. M. C. 1980 Separated flow models—I. Analysis of the averaged and local instantaneous formations. *Int. J. Multiphase Flow* **6**, 1–24.

BANERJEE, S., HUSSEIN, E. & MENELEY, D. A. 1979 Simulation of a neutron scattering method of measuring void fraction in two-phase flow. *Nucl. Eng. Design* **53**, 393–405.

BURRUS, W. R. 1965 Utilization of a Priori Information by Means of Mathematical Programming in Statistical Interpretation of Measured Distributions. ORNL-3743.

CHADAN, K. & SABATIER, P. C. 1977 *Inverse Problems in Quantum Theory*. Springer-Verlag, New York.

CURTAIN, R. F. & PRITCHARD, A. J. 1977 *Functional Analysis in Modern Applied Mathematics*. Academic, New York.

FORIST 1975 Neutron Spectrum Unfolding Code–Iterative Smoothing Technique. RSIC, ORNL, PSR-92.

HAU, K. & BANERJEE, S. 1981 Measurement of mass flux in two-phase flow using combinations of pitot tubes and gamma densitometers. *AIChE J.* **27**, 177–184.

HENRY, A. F. 1975 *Nuclear Reactor Analysis.* MIT Press, Cambridge, MA.

HUGHES, D. J. & SCHWARTZ, R. B. 1958 Neutron Cross Sections, BNL-325, 2nd Ed.

HUSSEIN, E. M. A. 1983 Fast Neutron Scattering Technique for Local Void Fraction Measurement in Two-Phase Flow. Ph.D. Thesis, McMaster University.

HUSSEIN, E. 1984 *New Trends in Neutron Diagnosis of Multiphase Flows. Multi-Phase Flow and Heat Transfer III, Part B: Applications* (Edited by T. V. Veziroglu and A. E. Bergles), pp. 795–810. Elsevier, Amsterdam.

HUSSEIN, E., BANERJEE, S. & MENELEY, D. A. 1983 New Fast Neutron Scattering Technique for Local Void Fraction Measurement in Two-Phase Flow. *Proc. 2nd Int. Topical Meeting on Nuclear Reactor Thermal-Hydraulics,* (Edited by M. Merlio), ANS. pp. 1431–1442.

HUSSEIN, E., BOT, D. L., BANERJEE, S. & MENELEY, D. A. 1984 Design aspects of a fast neutron scattering technique for phase distribution measurement in two-phase flow. *Measuring Techniques in Gas-Liquid Two-Phase Flows* (Edited by J. M. Delhaye and G. Cognet), pp. 359–399. Springer, Berlin.

HUSSEIN, E. & KONDIC, N. 1984 Radiation scattering techniques for density field measurement. A comparative study. *Mass Flow Measurements* (Edited by T. R. Heidrick), FED-Vol. 17, pp. 101–111. ASME, FED.

KONDIC, N., JACOBS, A. & EBERT, D. 1983 Three-Dimensional Density Field Determination by External Stationary Detectors and Gamma Sources Using Selective Scattering. *Proc. 2nd Int. Topical Meeting on Nuclear Reactor Thermal-Hydraulics* (Edited by M. Merilo), pp. 1443–1462. ANS.

KREYSZIG, E. 1978 *Introductory Functional Analysis with Applications.* Wiley, New York.

MILLER, K. 1970 Least-squares for ill-posed problems with a prescribed bound. *SIAM J. Math., Anal.* **1,** 52–74.

OSTROWSKI, A. M. 1966 *Solution of Equations and Systems of Equations.* Academic, New York.

PEREZ-GRIFFO, M. L., BLOCK, R. C. & LAHEY, R. J., JR. 1982 Measurement of flow in large pipes by the pulsed neutron activation method. *Nucl. Sci. Eng.* **82,** 19–33.

PERKINS, L. J. & SCOTT, M. C. 1979 The application of pulse shape discrimination in NE-213 to neutron spectroscopy. *Nucl. Instrum. Meth.* **166,** 451–464.

SABATIER, P. C. 1978 Introduction to applied inverse problems. Lecture notes in physics: *Applied Inverse Problems,* (Edited by P. C. Sabatier), pp. 1–23. Springer-Verlag, New York.

SAWYER, W. W. 1978 *A First Look at Numerical Functional Analysis.* Clarendon, Oxford.

TIKHONOV, A. N. & ARSENIN, V. Y. 1977 *Solution of Ill-Posed Problems.* Wiley, Toronto.

TOMS, M. E. 1971 A computer analysis to obtain neutron spectra from an organic scintillator. *Nucl. Instrum. Meth.* **92,** 61–70.

ZAKAIB, G. D., HARMS, A. A. & VLACHOPOULOS, J. 1978 Two-dimensional void reconstruction by neutron transmission. *Nucl. Sci. Eng.* **65,** 145–154.

APPENDIX A. CONDITIONS FOR CONVERGENCE OF THE SAP IN THE SENT PROBLEM

To examine the convergence of the SAP, the relationship [19] at any approximation $k + 1$ is viewed as a mapping $\mathbf{f}_k$ of the given approximation ρ_k to the sought approximation ρ_{k+1}, i.e.

$$\mathbf{f}_k : \rho_k \rightarrow \rho_{k+1}, \qquad [A1]$$

where

$$\mathbf{f}_k(\rho_k) = \mathbf{A}^{-1}(\rho_k)S. \qquad [A2]$$

Since ρ_k and ρ_{k+1} are both approximations to the actual solution ρ, and if one makes sure that both ρ_k and ρ_{k+1} belong to the set of solutions C, defined by the interval [0, 1], then the mapping ρ_k maps the set C into itself. The solution ρ is called the "fixed point" of the mapping **f** since

$$\mathbf{f}(\rho) = \rho;$$

that is, the image of ρ coincides with itself (ρ is kept fixed). This formulation of the SAP enables us to make use of the fixed point theorem (contraction theorem) to prove the convergence and uniqueness of the solution (see Kreyszig 1978; Curtain & Pritchard 1977, among others). The following version of the fixed point theorem is particularly useful for our problem.

Let B be a closed subset of complete metric space X and the mapping **f** of: $B \rightarrow B$ be such that

$$\| \mathbf{f}(\rho_x) - \mathbf{f}(\rho_y) \| \leqq \alpha \| \rho_x - \rho_y \|, \quad 0 \leqq \alpha \leqq 1, \qquad [A3]$$

for all $\rho_x, \rho_y \in B$. Then, there exists a unique ρ^* in B, such that

$$\mathbf{f}(\rho^*) = \rho^*.$$

Moreover, ρ^* (the fixed point) may be obtained as the limit of the sequence (ρ_n), where

$$\rho_n = \mathbf{f}(\rho_{n-1}), \rho_0 \in B. \qquad [A4]$$

A lemma of the theorem states (Kreyszig 1978): A contraction mapping on a metric space is a continuous mapping.

To apply the above theorem and its lemma on the SENT problem, one needs a complete metric space, a contraction mapping on it, and a closed ball. To define a metric space one needs a set and a metric on it. We take the set X of all N-dimensional vectors of real numbers (clearly the set C of the solution vectors, ρ, is a subset of X, since ρ is an N-component vector of real numbers, water fractions, in the closed interval [0, 1]). On X we define a metric d by

$$d(\mathbf{x}, \mathbf{y}) = \max_j |x_j - y_j|, \qquad [A5]$$

where x_j and y_j are the jth components of the vectors **x** and **y**, respectively, and both vectors belong to the set X. The space $X = (\mathbf{x}, d)$ is complete; for the proof see Sawyer (1978). The closed ball in the SENT problem is simply the set C defined by the closed interval [0, 1], since it forms a closed subset of X and any closed set is also a closed ball, (Kreyszig 1978). Now in order to make use of the fixed point theorem, one has to prove that **f** is a contraction mapping within the [0, 1] interval.

To obtain the mathematical conditions for contraction mapping, consider the mapping **f** of [A2]:

$$\mathbf{f}_{k+1} = \mathbf{A}_k^{-1}S, \qquad [A6]$$

where **A** and S are as defined in section 2 and the subscript k indicates that **A** is evaluated using the vector $\rho_k = \mathbf{f}_{k-1}$. The conditions for contraction mapping of $\mathbf{f}$ are

$$\| \mathbf{f}_{k+1} - \mathbf{f}_k \| \leq \alpha \| \rho_k - \rho_{k-1} \|, \quad 0 \leq \alpha < 1, \quad k = 1, 2, \ldots \qquad \text{[A7]}$$

Using the mean-value theorem, one can write

$$\mathbf{f}_{k+1} - \mathbf{f}_k = \mathbf{J}_k \cdot (\rho_k - \rho_{k-1}), \qquad \text{[A8]}$$

where $\mathbf{J}_k$ is the Jacobi matrix of partial derivative of $\mathbf{f}$ with respect to ρ, estimated at a value $\bar{\rho} \epsilon [\rho_{k-1}, \rho_k]$. Therefore,

$$\| \mathbf{f}_{k+1} - \mathbf{f}_k \| \leq \| \mathbf{J}_k \| \cdot \| \rho_k - \rho_{k-1} \|. \qquad \text{[A9]}$$

The jth row of the $\mathbf{J}_k$ matrix is given by

$$\begin{aligned} \mathbf{J}^T_{k,j} &= \frac{\partial}{\partial \rho_j} (\mathbf{A}^{-1} S) \\ &= \mathbf{A}^{-1} \frac{\partial}{\partial \rho_j} \mathbf{A}^{-1} S, \end{aligned} \qquad \text{[A10]}$$

where ρ_j is the jth element of the vector ρ. Using [4] of the paper, then

$$\begin{aligned} \mathbf{J}_{k,j} &\leq \mathbf{A}^{-1} \beta_j \mathbf{A} \mathbf{A}^{-1} S \\ &\leq | \beta_j | \mathbf{A}^{-1} S = | \beta_j | \bar{\rho}_k, \quad j = 1, 2, \ldots, N, \end{aligned} \qquad \text{[A11]}$$

where β_j is the maximum absolute value of the coefficients of the exponential terms of the elements of $\mathbf{A}$ in which ρ_j appears, and is equivalent to the maximum distance in mean-free paths a neutron travels in cell j. In the above equation, $\bar{\rho}_k$ is substituted for $\mathbf{A}^{-1} S$ since the Jacobi matrix is to be evaluated at $\bar{\rho}_k$. Now one can write the inequality

$$| \mathbf{J}_k | \leq N | \beta | \, \| \rho_k \|, \qquad \text{[A12]}$$

where N is the dimension of ρ and also is the number of rows in $\mathbf{J}_k$, and

$$| \beta | = \max_j | \rho_j |. \qquad \text{[A13]}$$

Using the inequalities [A9] and [A12], the contraction mapping condition [A7] can be restated as

$$0 \leq N | \beta | \, \| \bar{\rho}_k \| \leq \alpha < 1.$$

Since $\bar{\rho}_k \epsilon [\rho_{k-1}, \rho_k]$ and in the successive approximation process ρ_{k-1} and $\rho_k \epsilon [0,1]$ (if not, they are adjusted before starting the new iteration), and using the norm defined by [A4], then $\| \bar{\rho} \| \leq 1$. Therefore, [A13] can be rewritten as

$$0 \leq N | \beta | \leq \alpha < 1, \qquad \text{[A14]}$$

as the condition for $\mathbf{f}$ to be contraction mapping, where $| \beta |$ as defined by [A13] is the maximum distance in mean-free paths a neutron travels in any cell.

The condition [A14] requires the value of $| \beta |$ to be much less than unity, since the number N (number of unknowns), is usually large. However, if one defines a mapping $\mathbf{f}^c$

such that

$$\mathbf{f}^c_{k+1} = (c\rho_k - \mathbf{f}_{k-1}) \,/\, (c - 1), \qquad \text{[A15]}$$

where c is a positive constant, then the contraction mapping conditions can be relaxed, while the solution of the problem does not change. This is because when the solution ρ is reached, both ρ_k and $\mathbf{f}_{k+1}$ approach ρ, and according to [A15], also $\mathbf{f}^c_k$ approaches ρ. Therefore, the mapping $\mathbf{f}_c$ is a self mapping of ρ and the fixed point theorem is still applicable. The conditions for the contraction of $\mathbf{f}^c$ are

$$\| \mathbf{f}^c_{k+1} - \mathbf{f}^c_k \| \leqq \alpha \, \| \rho_k - \rho_{k-1} \|, \quad k = 0, 1, 2, \ldots \qquad \text{[A16]}$$

But,

$$\begin{aligned} \| \mathbf{f}^c_{k+1} - \mathbf{f}^c_k \| &= \| c\rho_k - \mathbf{f}_{k+1} - c\rho_{k-1} - \mathbf{f}_k \| \,/\, (c - 1) \\ &= c \, \| (\rho_k - \rho_{k+1}) - (\mathbf{f}_{k+1} - \mathbf{f}_k) \, c^{-1} \| / (c - 1) \\ &\leqq \| \rho_k - \rho_{k-1} \| \cdot \| \mathbf{f}_{k+1} - \mathbf{f}_k \| \,/\, (c - 1) \\ &\leqq | \beta | \, N \,/\, (c - 1) \cdot \| \rho_k - \rho_{k-1} \|, \end{aligned} \qquad \text{[A17]}$$

by employing inequalities [A9], [A10] and [A13] in the last line.

From inequalities [A16] and [A17], one can conclude that the contraction mapping of $\mathbf{f}^c$ requires

$$0 < | \beta | \, N \,/\, (c - 1) \leqq \alpha < 1. \qquad \text{[A18]}$$

By choosing an appropriate value for c, usually larger than unity, the conditions of [A18] become more relaxed compared to those of [A14]. In the SENT problem, c is taken equal to the number of unknowns, N. If N is sufficiently large, then condition [A18] can be reduced to

$$0 \leqq \beta \leqq \alpha < 1. \qquad \text{[A19]}$$

Subsection 4.2 of the paper shows the physical conditions under which β satisfies the above inequality.

The formulation of $\mathbf{f}^c$ according to [A15] was suggested by Ostrowski (1966) for insuring and improving the convergence of nonlinear iterations.